

## Coalescence and Secondary Ice Development in Cumulus Congestus Clouds

R. PAUL LAWSON,<sup>a</sup> ROELOF BRUINJTJES,<sup>b</sup> SARAH WOODS,<sup>a</sup> AND COLIN GURGANUS<sup>a</sup>

<sup>a</sup> SPEC Inc., Boulder, Colorado

<sup>b</sup> National Center for Atmospheric Research, Boulder, Colorado

(Manuscript received 11 July 2021, in final form 15 December 2021)

**ABSTRACT:** Understanding ice development in cumulus congestus (CuCg) clouds, which are ubiquitous globally, is critical for improving our knowledge of cloud physics, precipitation and climate prediction models. Results presented here are representative of data collected in 1008 penetrations of moderate to strong updrafts in CuCg clouds by five research aircraft in six geographic locations. The results show that CuCg with warm ( $\sim 23^{\circ}\text{C}$ ) cloud-base temperatures, such as in tropical marine environments, experience a strong collision–coalescence process. Development of coalescence is also correlated with drop effective radius  $> \sim 12$  to  $14\ \mu\text{m}$  in diameter. Increasing the cloud-base drop concentration with diameters from  $15$  to  $35\ \mu\text{m}$  and decreasing the drop concentration  $< 15\ \mu\text{m}$  appears to enhance coalescence. While the boundary layer aerosol population is not a determinate factor in development of coalescence in most tropical marine environments, its impact on coalescence is not yet fully determined. Some supercooled large drops generated via coalescence fracture when freezing, producing a secondary ice process (SIP) with production of copious small ice particles that naturally seed the cloud. The SIP produces an avalanche effect, freezing the majority of supercooled liquid water before fresh updrafts reach the  $-16^{\circ}\text{C}$  level. Conversely, CuCg with cloud-base temperatures  $\leq \sim 8^{\circ}\text{C}$  develop significant concentrations of ice particles at colder temperatures, so that small supercooled water drops are lofted to higher elevations before freezing. Recirculation of ice in downdrafts at the edges of updrafts appears to be the primary mechanism for development of precipitation in CuCg with colder cloud-base temperatures.

**SIGNIFICANCE STATEMENT:** Cumulus congestus clouds occur globally and account for a significant amount of precipitation in the tropics. The physics underlying the warm rain process and development of ice in cumulus congestus clouds are fundamental to a better understanding of precipitation formation. The collected data show that the strength of collision–coalescence is strongly influenced by cloud-base temperature, and that millimeter-diameter supercooled cloud drops will form in convective clouds with base temperatures warmer than  $20^{\circ}\text{C}$ . When supercooled large drops form, there is a secondary ice process that rapidly freezes the large majority of supercooled cloud water before updrafts reach the  $-16^{\circ}\text{C}$  level. Incorporating results from the observations will improve cloud-resolving and climate prediction models.

**KEYWORDS:** Aerosols; Climate prediction; Cloud droplets; Cumulus clouds; Glaciation; Ice particles; Mixed precipitation; Thermodynamics

### 1. Introduction

Cumulus congestus (CuCg) clouds are ubiquitous globally and make substantial contributions to precipitation and latent heat fluxes in the tropics (Wall et al. 2013). CuCg produced 57% of the precipitation occurring from convective clouds in the Tropical Ocean and Global Atmosphere Coupled Ocean–Atmosphere Response Experiment (TOGA COARE), and 28% of the total convective rainfall over the west Pacific warm pool (Johnson et al. 1999).

Primary nucleation in CuCg occurs when an ice nucleating particle (INP), i.e., a small aerosol particle with nucleating properties, induces a supercooled water drop to freeze. A long-standing enigma in cloud physics research is that aircraft

measurements of INP concentrations are orders of magnitude less than measurements of ice particles (IPs) in CuCg with cloud-top temperatures  $\geq \sim -12^{\circ}\text{C}$  (Bigg 1973; DeMott et al. 2016; Lasher-Trapp et al. 2016). DeMott et al. (2016) collected both airborne and ground-based measurements of the activation temperatures of INPs during the Ice in Clouds Experiment–Tropical (ICE-T), staged out of Saint Croix in 2011. Their measurements show that INPs were present in concentrations of about  $10^{-4}\ \text{L}^{-1}$  at  $-12^{\circ}\text{C}$ , and the warmest temperature that INPs were found to be active was  $-6^{\circ}\text{C}$ , in concentrations of about  $2 \times 10^{-5}\ \text{L}^{-1}$ . In contrast, Lawson et al. (2015) show measurements of IPs that range from hundreds to thousands per liter in updrafts of growing ICE-T CuCg. Koenig (1963, 1965) postulated that the breakup of supercooled millimeter-diameter drops in concentrations of  $\sim 50\ \text{m}^{-3}$  was responsible for ice multiplication in CuCg in southern Missouri. The cloud-base elevations were 3500–5000 ft ( $\sim 1000$ – $1500\ \text{m}$ ;  $\sim 18^{\circ}$  to  $20^{\circ}\text{C}$ ) with tops about  $-10^{\circ}\text{C}$ . Lawson et al. (2015) also associated high concentration of IPs with coalescence and a secondary ice process (SIP) that

---

Gurganus's current affiliation: NOAA/Chemical Sciences Laboratory, Boulder, Colorado.

---

Corresponding author: Paul Lawson, plawson@specinc.com

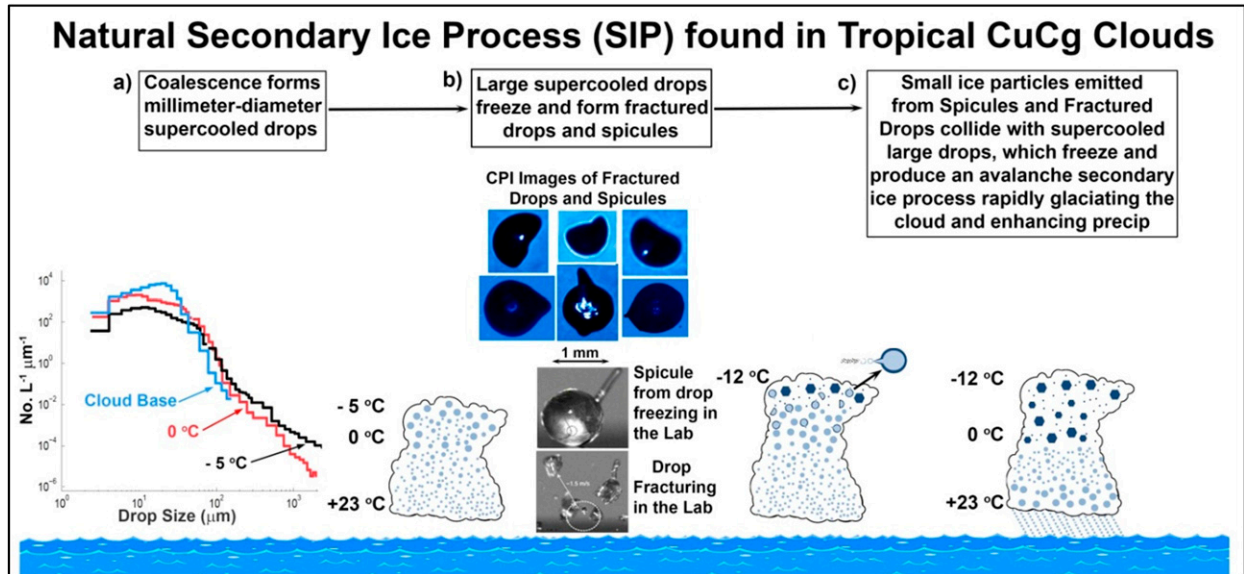


FIG. 1. Illustration showing how the natural secondary ice process (SIP) operates in tropical marine cumulus congestus clouds. (a) DSDs progressing from cloud base to the  $-5^{\circ}\text{C}$  level in all-liquid updrafts. (b) Depiction of fracturing of SLDs in the region from  $-12^{\circ} \leq T \leq -6^{\circ}\text{C}$  with examples of in situ CPI images of frozen fractured drops and spicules. High-speed photography shows a drop freezing in the laboratory and producing a spicule (Wildeman et al. 2017). (c) Rapid freezing of the supercooled region of cloud due to “seeding” from the avalanche SIP created by freezing of SLDs.

resulted from the fracturing of supercooled large drops (SLDs), sometimes via formation of spicules<sup>1</sup> that emitted small IPs.

Lawson et al. (2017) extended the measurements to other geographic locations, including over the Gulf of Mexico, over land in the southeast United States (SEUS) and over the High Plains in the western United States. Their measurements indicate that warm cloud-base temperatures (i.e., the depth of warm cloud) is a critical factor in the development of coalescence, which is associated with a SIP that results when SLDs freeze and fracture. In CuCg with cloud-base temperature  $\geq 20^{\circ}\text{C}$  and drop concentration  $< \sim 700 \text{ cm}^{-3}$  the SIP is active and the majority of supercooled liquid water (SLW) is frozen before the updrafts reach the  $-16^{\circ}\text{C}$  level (Lawson et al. 2015, 2017). Conversely, in CuCg with cloud-base temperatures  $< -8^{\circ}\text{C}$ , several studies have shown that small ( $< \sim 200 \mu\text{m}$ ) supercooled drops are lofted to much colder temperatures (e.g., Heymsfield et al. 1978, 1979; Lawson et al. 2017).

Figure 1 is an illustration showing how coalescence and the hypothetical SIP proceed in CuCg with cloud-base temperatures  $\geq 20^{\circ}\text{C}$ , where SLDs freeze, fracture and produce ice fragments and/or spicules. The drop-fracturing and spicule production processes have been observed in the laboratory, as illustrated in Fig. 1b, resulting in the generation of small IPs (Lauber et al. 2018; Wildeman et al. 2017; Korolev and

Leisner 2020; Keinert et al. 2020). In the supercooled regions of CuCg, IPs that are emitted from spicules and pieces of frozen fractured drops collide with other SLDs, generating an avalanche process that rapidly freezes the majority of SLW in the cloud. The rapid freezing process is facilitated by the difference in terminal velocities of the SLDs and small IPs. Lawson et al. (2015) developed a numerical model suggesting that this process could account for the rapid freezing of SLW in the temperature region from  $-20^{\circ}$  to  $-12^{\circ}\text{C}$  in ICE-T CuCg.

In this paper we show that CuCg with cloud-base temperatures  $\geq 20^{\circ}\text{C}$  and drop concentrations  $< \sim 700 \text{ cm}^{-3}$  all form SLDs via a collision-coalescence process. New measurements suggest that the boundary layer aerosol size distribution does not have a dominant impact on the formation of coalescence, but that it likely influences the strength of coalescence development and the SIP in these warm-base clouds. We emphasize that this paper focuses primarily on the microphysical conditions producing (and not producing) coalescence, which has been shown in Lawson et al. (2015, 2017) to generate a SIP based on drop fracturing observed in laboratory experiments (Lauber et al. 2018; Wildeman et al. 2017; Korolev and Leisner 2020; Keinert et al. 2020). Section 2 discusses instrumentation and sampling methodology used by the research aircraft. In section 3 we present new measurements collected in the United Arab Emirates (UAE) and over the South China and Philippine Seas in 2019. Section 4 synthesizes and generalizes the results from six geographic locations. We present a summary and discussion of results in section 5. The results presented here can be used in parameterizations of cloud-resolving and climate models to improve predictions of rain and cloud radiative forcing.

<sup>1</sup> A spicule is a spike protruding from a frozen drop that occurs upon freezing due to increased pressure inside the drop; this phenomenon is often seen in ice trays in a kitchen freezer. Laboratory experiments have shown that minute particles may be ejected through a hollow spicule in a freezing drop (Fig. 1).

## 2. Instrumentation and methodology

Airborne measurements were collected in six geographic locations using five research aircraft, including two Stratton Park Engineering Company (SPEC) Inc. Learjets, the National Aeronautics and Space Administration (NASA) DC-8 and P-3B aircraft, and a C-130 owned by the National Science Foundation (NSF) and operated by the National Center for Atmospheric Research (NCAR). All aircraft were equipped with a suite of state-of-the-art microphysical sensors. The Learjet was equipped with a passive cavity aerosol spectrometer probe (PCASP) (Cai et al. 2013), a fast forward scattering spectrometer probe (FFSSP) (O'Connor et al. 2008; Lawson et al. 2017), a fast cloud droplet probe (FCDP) (Woods et al. 2018; Lawson et al. 2017), a Nevzorov liquid and total water content device (Korolev et al. 1998), a 2D-stereo (2D-S) optical array probe (OAP) (Lawson et al. 2006), a 3-view cloud particle imager (3V-CPI) (Lawson et al. 2001) with 10- and 50- $\mu\text{m}$  OAPs, and a high volume precipitation spectrometer probe (HVPS) (Lawson et al. 1998). Image data were processed using the methodology explained in an appendix found in Lawson et al. (2017). The P-3B was equipped with the same microphysical probes except for the FFSSP. The NCAR C-130 was equipped with its standard suite of aerosol and cloud probes. C-130 FSSP and air motion data were used in the measurements of cloud-base drop size distributions (DSDs), as shown in Lawson et al. (2015). Air motions were recorded on the Learjet using an aircraft integrated meteorological measurement system (AIMMS-20) (Beswick et al. 2008) and inertial navigation systems on the other aircraft.

Data were collected from 1008 penetrations of CuCg in six locations: north of Saint Croix over the Caribbean Sea during the NSF ICE-T experiment in 2011; in the SEUS during the 2013 Studies of Emissions, Atmospheric Composition, Clouds and Climate Coupling by Regional Surveys (SEAC<sup>4</sup>RS) project; Texas Panhandle (Amarillo, Texas); High Plains (Colorado, Wyoming, Nebraska) during the 2015–17 UAE Rain Enhancement Program (UAEREP); the UAEREP 2019 program in the UAE; and during the 2019 NASA Cloud, Aerosol and Monsoon Processes Philippines Experiment (CAMP<sup>2</sup>Ex) project over the South China and Philippine Seas. Lawson et al. (2015, 2017) provide more detailed microphysical descriptions of CuCg in the Caribbean, Gulf of Mexico, SEUS, and midlatitudes.

Measurements of temperature and pressure were collected in noncloudy air immediately below or at the level of cloud base. DSDs measured within a few hundreds of meters above cloud base are called “cloud-base penetrations.” The region within a few hundreds of meters above cloud base is selected because this is where the large majority of cloud condensation nuclei (CCN) have activated and formed detectable water drops (Fitzgerald 1972; Pruppacher and Klett 1997). The NCAR C-130 (ICE-T project) and NASA P-3B (CAMP<sup>2</sup>Ex) often sampled near cloud base while the Learjet sampled growing turrets<sup>2</sup> in the supercooled region of cloud.

<sup>2</sup> A “turret” is a cumulus tower that has a top with a cauliflower appearance.

The onboard scientist targeted CuCg clouds that were fresh (i.e., with a cauliflower top), growing, and did not appear to be contaminated by neighboring or higher clouds. “Cloud top” penetrations were typically conducted about 300 m below visible cloud top. CPI and 2D-S images collected in updrafts that are identified as “all liquid” and/or “ice-free” have been examined to determine that they were not contaminated with precipitation falling from above, or ice being mixed in from adjacent downdrafts. DSDs and ice particle size distributions (PSDs) are generated by separating water drops and IPs using CPI and 2D-S images, as shown in Lawson et al. (2015).

## 3. Results

### a. UAEREP campaign

The SPEC Learjet flew ten missions staged out of Al Ain International Airport in the UAE during August 2019. The majority of flights were conducted near the western foothills of the Al Hajar mountains, where most of the CuCg formed in the late morning to early afternoon. Figure 2a shows the location of first echoes from dual-polarimetric 5-cm-radar data recorded in 2016, which were used for planning the 2019 field project. The histogram in Fig. 2b shows that the first radar echoes were most likely to form during the month of August. The histogram in Fig. 2c indicates that first echoes typically formed between 0900 and 1100 UTC (1100 and 1300 local time) during the June–October period, which also applies to the month of August. Figure 3 shows the Learjet flight tracks for the CuCg cloud missions in 2019. In all cases UAE air traffic control instructed the Learjet to depart Al Ain airport to the southwest and climb to 23 000 ft (7 km) before returning to investigate CuCg near the foothills of the Al Hajar Mountains. The location of CuCg in 2019 was similar to the first echo analysis in 2016 (Fig. 2a), as evidenced by the 2019 flight tracks shown in Fig. 3.

Four days, specifically 12, 13, 18, and 19 August 2019 produced CuCg that could be investigated from cloud base to cloud top. UAE air traffic control limited the altitude of the Learjet to 23 000 ft (7 km), which corresponded to about the  $-16^{\circ}\text{C}$  level. Figure 4 shows DSDs from cloud-base penetrations on the 4 days of interest. The four DSDs are very similar with drop concentrations from 441 to 797  $\text{cm}^{-3}$  that extend out to 100  $\mu\text{m}$ . The 12 August case is selected here as a typical example of investigations of CuCg during the UAEREP project. The temperature at cloud base was estimated to be  $10^{\circ}\text{C}$  based on Learjet measurements. The cloud-base DSDs are representative of the boundary layer aerosol population, shown in Fig. 5b, along with examples of CPI images of the aerosols.

The high concentration (799  $\text{cm}^{-3}$ ) of aerosols extending out to 100  $\mu\text{m}$  (Fig. 5b) is typical in the UAE. It is not possible to positively identify the CPI images in Fig. 5c, but based on images examined from other projects, the quasi-round images are probably sand particles and the larger stringlike images are likely bio material. Wehbe et al. (2021) report the

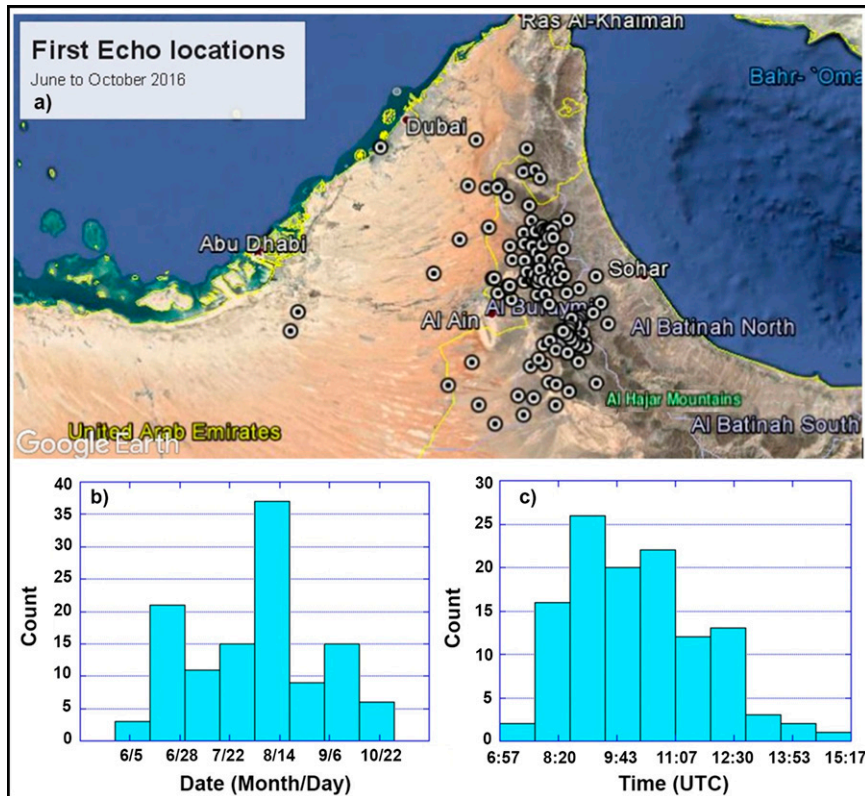


FIG. 2. (a) Location of first radar echoes (indicated by white outlined circle markers) from June–October 2016 over the western foothills of the Al Hajar mountains in the UAE. Also shown are histograms indicating the number of radar detectable storms as a function of (b) date and (c) time of day.

mean boundary layer PCASP particle concentrations from two flights (12 and 19 August) during the UAEREP project varied around  $500 \text{ cm}^{-3}$  and extended to diameters of  $100 \mu\text{m}$ , with higher variations (up to  $1000 \text{ cm}^{-3}$ ) during the

flight on 12 August 2019. Semeniuk et al. (2014) collected aerosol particles in ambient and updraft conditions of natural convection systems near the Al Hajar Mountains in 2002. They analyzed the samples using transmission electron

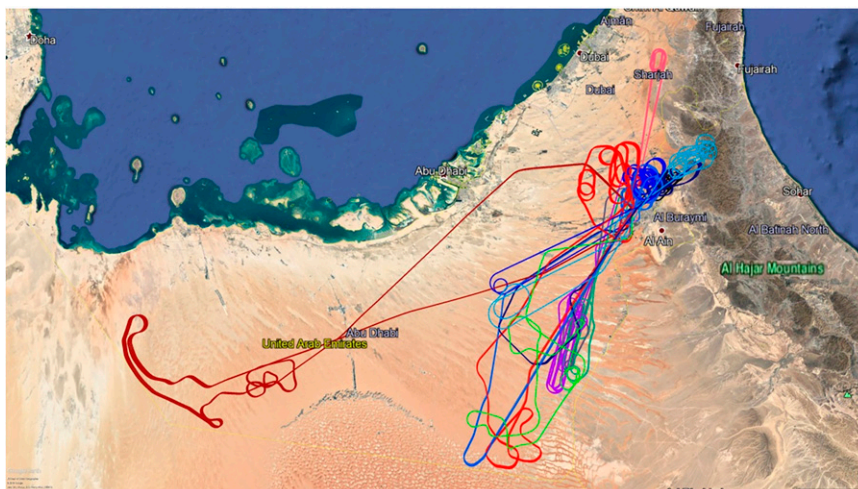


FIG. 3. Learjet flight tracks, where each color represents a different flight during the 2019 UAEREP project. The focus of operations was over the western foothills of the Al Hajar mountains.

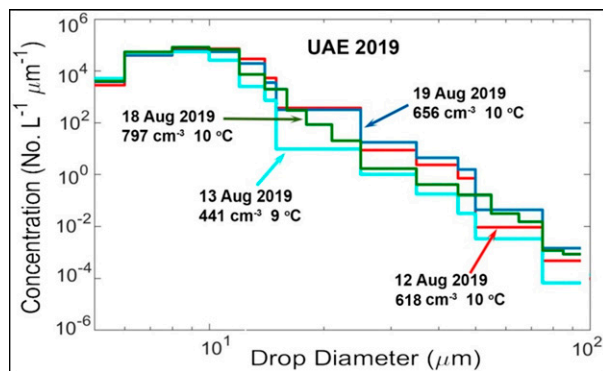


FIG. 4. Cloud-base drop size distributions (DSDs) that are a combination of FFSSP and 2D-S probes sampled by the Learjet during four UAERP cloud missions (12, 13, 18, and 19 Aug 2019).

microscopy and found that the fine-mode fraction comprised up to 90% mixed cation sulfate droplets, while the coarse fraction comprised up to 80% mineral-containing aggregates. Dry particles were typically silicate grains. Wet particles

were mineral aggregates with chloride, nitrate, or sulfate components, and droplets were mainly aqueous NaCl and mixed cation sulfate droplets. Their results show that soluble salts from local pollution and natural sources enhanced the spectrum of particles forming CCN, and by forming giant CCN from aggregates. [Wehbe et al. \(2021\)](#) show back trajectories at 1500 m that indicate advection of aerosols from the Arabian Sea. [Semeniuk et al. \(2014\)](#) found evidence of pollution from land sources. These studies suggest that the CCN are a combination of aerosols advected from the ocean and generated over land.

Despite the broad DSD at cloud base that contained giant (>1 μm) and ultragiant (>10 μm) aerosols ([Johnson 1982](#)), CuCg in the UAE did not develop a strong coalescence process. Measurements near the 0°C level showed that the maximum diameter drops reached only a few hundreds of microns. The very rare millimeter-diameter drops that were recorded in UAE CuCg were not observed until the -12°C level. The strength of the coalescence process in UAE CuCg and results from other locations are examined in more detail in [section 4a](#).

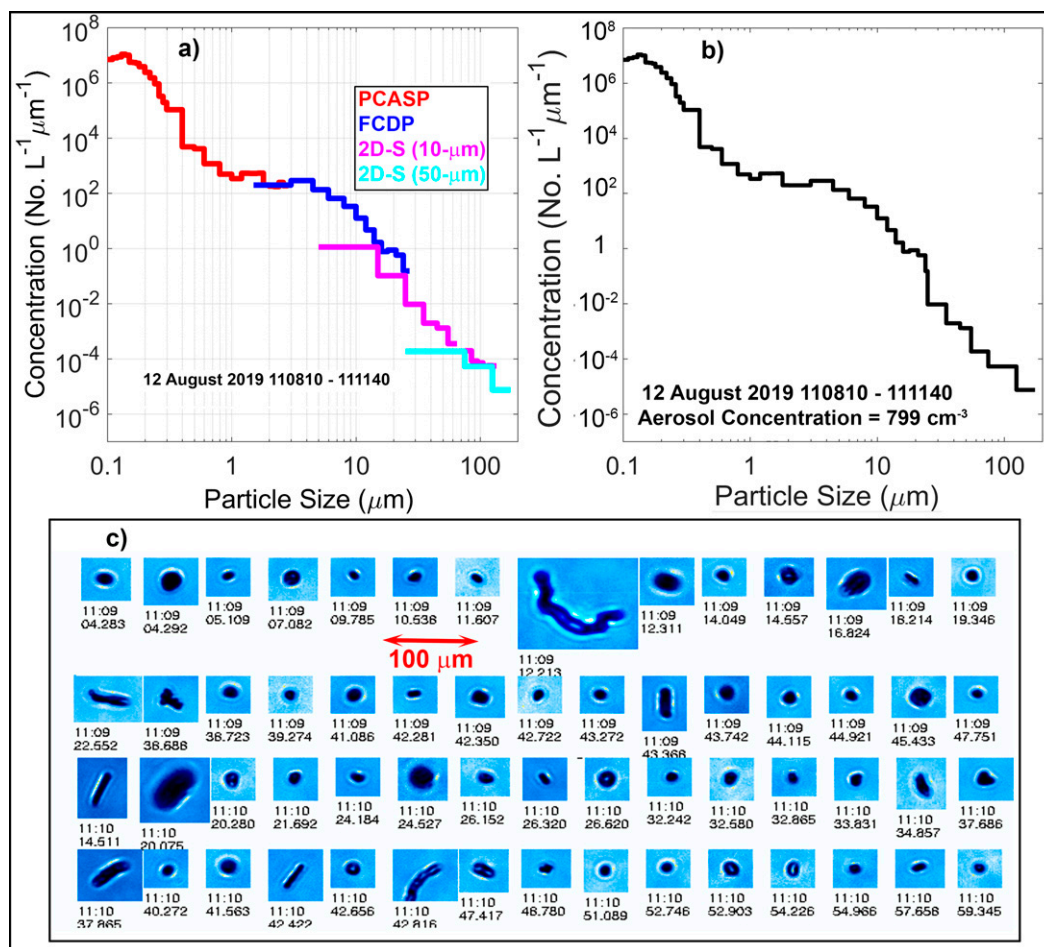


FIG. 5. Clear-air aerosol particle size distributions (PSDs) from data collected at 9.5°C in the UAE on 12 Aug 2012. (a) PSDs from individual particle probes, (b) a composite PSD from probes shown in (a), and (c) examples of CPI images of aerosol particles.

TABLE 1. Listing of mean values (except as noted) from 116 selected cloud passes in CuCg. LR refers to the Learjet and RF refers to the P-3B, with flight numbers following the designator. Start and end times extending past 2400:00 are shown as 2500:00, 2600:00, 2700:00, etc., on that day. VaV max is maximum 1-s vertical air velocity in cloud pass, Conc is concentration, LWC is liquid water content,  $R_{\text{eff}}$  is particle effective radius, and IWC is ice water content.

State and air motion parameters						Liquid			Ice	
Flight No.	Date	Start time (UTC)	End time (UTC)	Temp (°C)	VaV max (m s <sup>-1</sup> )	Conc (cm <sup>-3</sup> )	LWC (g m <sup>-3</sup> )	$R_{\text{eff}}$ ( $\mu\text{m}$ )	Conc (cm <sup>-3</sup> )	IWC (g m <sup>-3</sup> )
Cloud-base region: 21.5° to 24.1°C										
LR02	9 Sep 2019	0215:17	0215:23	21.5	2.8	710	0.21	4.3	0	0
LR05	15 Sep 2019	0901:36	0901:38	21.5	3.7	360	0.46	7.1	0	0
RF12	21 Sep 2019	3011:23	3011:42	21.5	2.2	996	0.20	4.4	0	0
LR09	24 Sep 2019	0737:54	0738:00	21.6	2.8	740	0.77	6.2	0	0
LR01a	7 Sep 2019	0240:46	0240:56	21.8	2.7	449	0.59	7.2	0	0
RF03	29 Aug 2019	2717:50	2717:55	22.0	0.4	678	0.56	6.4	0	0
RF04	30 Aug 2019	2537:14	2537:16	22.0	-999	431	0.26	5.8	0	0
RF08	13 Sep 2019	2329:33	2329:35	22.1	1.0	274	0.50	7.9	0	0
RF12	21 Sep 2019	2543:10	2543:16	22.3	1.0	899	0.19	4.1	0	0
RF16	29 Sep 2019	0355:51	0355:53	22.3	0.6	107	0.25	9.6	0	0
LR06a	17 Sep 2019	0208:59	0209:01	22.5	0.8	109	0.08	6.9	0	0
RF13	23 Sep 2019	2752:43	2753:03	22.5	2.4	1312	0.32	4.2	0	0
RF13	23 Sep 2019	2756:05	2756:10	22.5	1.3	1360	0.38	4.5	0	0
RF13	23 Sep 2019	2758:05	2758:07	22.5	1.5	1384	0.36	4.4	0	0
RF14	25 Sep 2019	0755:44	0755:49	22.6	0.6	328	0.13	4.9	0	0
RF14	25 Sep 2019	0756:15	0756:19	22.6	1.3	369	0.14	5.0	0	0
RF17	1 Oct 2019	2510:58	2511:01	22.6	2.1	917	0.46	5.4	0	0
RF10	16 Sep 2019	2538:03	2538:05	22.8	0.5	270	0.05	3.9	0	0
RF08	13 Sep 2019	2524:52	2524:56	23.0	2.4	286	0.36	7.1	0	0
RF08	13 Sep 2019	2525:57	2526:00	23.0	2.9	307	0.34	7.0	0	0
RF12	21 Sep 2019	2437:46	2437:58	23.0	1.4	393	0.14	4.9	0	0
RF12	21 Sep 2019	3012:48	3012:50	23.0	0.9	737	0.15	3.9	0	0
RF19	5 Oct 2019	0527:47	0527:49	23.0	1.9	385	0.22	5.4	0	0
RF19	5 Oct 2019	0528:59	0529:03	23.0	2.5	321	0.19	5.6	0	0
RF15	27 Sep 2019	2322:30	2322:36	23.1	1.9	130	0.45	9.7	0	0
RF15	27 Sep 2019	2325:41	2325:47	23.1	2.1	140	0.63	11.1	0	0
RF19	5 Oct 2019	0348:16	0348:21	23.1	2.3	88	0.40	10.7	0	0
RF19	5 Oct 2019	0351:04	0351:08	23.1	2.1	80	0.55	12.2	0	0
RF19	5 Oct 2019	0530:35	0530:41	23.1	1.9	169	0.25	7.3	0	0
RF19	5 Oct 2019	0339:08	0339:11	23.2	1.3	74	0.13	7.8	0	0
RF03	29 Aug 2019	2718:22	2718:26	23.3	2.5	936	0.27	4.5	0	0
RF17	1 Oct 2019	2415:52	2416:00	23.4	1.2	463	0.16	4.8	0	0
RF02	27 Aug 2019	0307:12	0307:20	23.5	3.3	671	0.60	6.4	0	0
RF02	27 Aug 2019	0314:11	0314:18	23.5	2.7	1102	0.46	5.2	0	0
RF03	29 Aug 2019	2718:04	2718:15	23.5	2.5	829	0.25	4.6	0	0
RF08	13 Sep 2019	2518:41	2518:54	23.5	2.6	273	0.31	6.9	0	0
RF17	1 Oct 2019	2539:25	2539:39	23.6	1.5	1007	0.21	4.0	0	0
RF17	1 Oct 2019	2539:12	2539:19	23.7	1.3	992	0.19	3.9	0	0
RF09	15 Sep 2019	2800:05	2800:11	24.1	1.1	1221	0.22	3.9	0	0
Mean values				22.8	1.8	572	0.32	6.1		
Warm cloud region: 3.1° to 21.1°C										
RF14	25 Sep 2019	0650:37	0650:43	3.1	6.7	84	1.9	23.4	0	0
RF14	25 Sep 2019	0650:50	0650:52	3.5	6.4	56	2.9	36.1	0	0
LR02	9 Sep 2019	0152:55	0152:58	5.1	4.8	76	2.1	29.6	0	0
LR01b	7 Sep 2019	0635:53	0635:55	5.1	9.1	184	2.0	19.2	0	0
LR01b	7 Sep 2019	0635:19	0635:21	5.5	11.8	514	5.0	15.7	0	0
LR09	24 Sep 2019	0715:01	0715:04	5.5	4.9	122	1.2	18.0	0	0
LR09	24 Sep 2019	0709:24	0709:35	6.5	7.1	292	4.9	19.6	0	0
LR10	25 Sep 2019	0530:41	0530:42	6.7	4.2	232	3.6	18.1	0	0
RF13	23 Sep 2019	2704:53	2705:03	9.0	3.5	532	3.9	14.2	0	0
RF13	23 Sep 2019	2707:21	2707:24	9.7	3.8	137	1.9	17.2	0	0
LR01a	7 Sep 2019	0232:00	0232:06	9.8	12.6	300	5.3	18.5	0	0

TABLE 1. (Continued)

State and air motion parameters						Liquid			Ice	
Flight No.	Date	Start time (UTC)	End time (UTC)	Temp (°C)	VaV max (m s <sup>-1</sup> )	Conc (cm <sup>-3</sup> )	LWC (g m <sup>-3</sup> )	R <sub>eff</sub> (μm)	Conc (cm <sup>-3</sup> )	IWC (g m <sup>-3</sup> )
LR01a	7 Sep 2019	0331:03	0331:06	9.9	7.4	201	2.6	17.1	0	0
LR01a	7 Sep 2019	0333:50	0333:57	10.5	14.7	646	4.7	13.6	0	0
LR09	24 Sep 2019	0727:28	0727:36	10.6	5.9	245	1.3	13.2	0	0
LR07	20 Sep 2019	0258:02	0258:04	11.3	4.6	386	3.3	14.6	0	0
LR01a	7 Sep 2019	0121:12	0121:16	12.1	4.1	198	3.2	19.9	0	0
LR01a	7 Sep 2019	0121:46	0124:54	13.0	11.7	267	3.4	18.9	0	0
LR02	9 Sep 2019	0203:00	0203:06	13.3	5.9	245	1.7	13.7	0	0
LR07	20 Sep 2019	0325:07	0325:11	13.5	4.9	259	1.3	12.8	0	0
LR07	20 Sep 2019	0326:57	0326:59	14.5	2.4	323	2.9	14.7	0	0
LR02	9 Sep 2019	0313:16	0313:20	15.3	3.1	248	2.2	14.7	0	0
RF13	23 Sep 2019	2734:23	2734:30	15.4	6.2	547	1.8	11.1	0	0
RF12	21 Sep 2019	2944:06	2944:24	17.8	8.1	868	1.3	8.3	0	0
RF01	24 Aug 2019	2725:15	2725:18	17.9	4.2	314	1.9	12.8	0	0
LR02	9 Sep 2019	0207:03	0207:11	18.1	7.5	289	1.1	10.9	0	0
LR01a	7 Sep 2019	0142:51	0142:55	19.0	4.8	334	1.3	11.1	0	0
RF01	24 Aug 2019	2420:58	2421:09	19.4	2.2	292	1.8	12.6	0	0
RF01	24 Aug 2019	2712:15	2712:21	20.9	5.1	387	1.2	9.7	0	0
RF01	24 Aug 2019	2702:49	2702:55	21.1	3.7	363	1.1	9.7	0	0
Mean values				11.8	6.3	308	2.5	16.2		
Ice-free region: within ±3°C of 0°C level										
RF06	6 Sep 2019	2624:59	2625:04	-3.0	6.0	93	1.7	36.8	0	0
RF03	29 Aug 2019	2356:49	2356:53	-3.0	11.3	14	2.5	71.8	0	0
RF16	29 Sep 2019	0732:26	0732:41	-2.8	5.9	37	1.5	54.9	0	0
RF03	29 Aug 2019	2348:45	2348:51	-2.5	5.1	35	0.9	38.0	0	0
RF03	29 Aug 2019	2348:56	2357:02	-2.5	4.6	39	2.1	41.3	0	0
RF03	29 Aug 2019	2350:27	2350:47	-2.5	5.4	33	1.6	94.2	0	0
RF03	29 Aug 2019	2356:27	2356:52	-2.5	11.3	24	3.0	70.7	0	0
RF06	6 Sep 2019	2619:37	2619:49	-2.1	7.2	67	2.4	60.0	0	0
RF07	8 Sep 2019	2527:43	2527:45	-2.1	5.1	40	1.4	36.3	0	0
LR05	15 Sep 2019	0840:01	0840:08	-2.0	8.2	20	2.2	59.3	0	0
LR05	15 Sep 2019	0834:46	0834:51	-1.6	11.3	45	1.6	40.0	0	0
LR05	15 Sep 2019	0839:19	0839:27	-1.0	7.6	20	2.8	91.2	0	0
RF19	5 Oct 2019	0643:46	0643:49	-1.0	7.1	43	1.7	62.1	0	0
LR01b	7 Sep 2019	0731:59	0732:12	-0.5	6.0	117	2.1	42.6	0	0
LR04	13 Sep 2019	0701:50	0702:00	0.0	10.0	18	2.2	75.5	0	0
LR06b	17 Sep 2019	0626:04	0626:11	0.0	9.0	12	2.0	55.5	0	0
RF10	16 Sep 2019	2827:12	2827:25	0.1	8.7	81	2.8	45.0	0	0
LR06b	17 Sep 2019	0545:27	0545:31	0.2	5.5	23	1.2	47.7	0	0
LR01a	7 Sep 2019	0323:41	0323:52	0.5	16.6	120	1.7	29.5	0	0
LR10	25 Sep 2019	0602:08	0602:13	0.6	9.2	62	2.1	42.7	0	0
LR01b	7 Sep 2019	0751:38	0751:46	1.0	18.5	166	3.4	28.2	0	0
LR10	25 Sep 2019	0602:08	0602:16	1.0	9.2	60	1.9	39.6	0	0
RF10	16 Sep 2019	2840:49	2840:56	1.1	7.4	74	1.2	19.8	0	0
RF10	16 Sep 2019	2826:12	2826:15	1.3	6.5	110	2.1	22.2	0	0
RF10	16 Sep 2019	2840:35	2840:47	1.3	7.4	75	1.5	22.1	0	0
LR02	9 Sep 2019	0148:08	0148:10	1.8	8.8	71	2.2	32.7	0	0
RF10	16 Sep 2019	2845:12	2845:22	1.8	5.0	65	1.4	22.9	0	0
LR06b	17 Sep 2019	0527:20	0527:31	2.1	5.6	29	3.7	86.9	0	0
LR05	15 Sep 2019	0842:59	0843:02	2.5	7.6	119	2.5	23.9	0	0
Mean values				-0.5	8.2	59	2.0	48.0		
Mixed-phase region: -16° to 12°C										
LR06a	17 Sep 2019	0130:17	0131:02	-16.0	7.3	15.8	0.104	46.1	435	1.66
RF03	29 Aug 2019	2749:11	2749:26	-15.6	2.5	0.2	0.003	51.9	446	1.30
LR09	24 Sep 2019	0756:24	0756:40	-15.3	2.2	0.3	0.001	57.8	137	0.79
RF06	6 Sep 2019	3033:42	3033:59	-14.3	5.5	17.3	0.058	51.4	167	1.28

TABLE 1. (Continued)

State and air motion parameters						Liquid			Ice	
Flight No.	Date	Start time (UTC)	End time (UTC)	Temp (°C)	VaV max (m s <sup>-1</sup> )	Conc (cm <sup>-3</sup> )	LWC (g m <sup>-3</sup> )	R <sub>eff</sub> (μm)	Conc (cm <sup>-3</sup> )	IWC (g m <sup>-3</sup> )
RF03	29 Aug 2019	2748:05	2748:43	-14.2	4.4	1.3	0.023	52.7	337	1.29
LR06a	17 Sep 2019	0125:46	0130:12	-14.2	16.8	5.2	0.600	51.3	111	1.03
RF06	6 Sep 2019	3032:58	3033:12	-14.1	5.0	27.9	0.082	38.4	204	0.78
RF06	6 Sep 2019	3034:01	3034:05	-14.1	3.2	2.0	0.016	57.0	332	1.60
RF06	6 Sep 2019	3049:51	3049:57	-14.0	1.3	0.2	0.000	62.3	107	1.05
RF06	6 Sep 2019	3034:07	3034:18	-13.9	2.5	2.0	0.012	59.1	317	1.44
RF19	5 Oct 2019	0629:59	0630:15	-13.6	0.5	1.6	0.038	66.1	68	1.09
LR02	9 Sep 2019	0356:22	0358:35	-13.4	3.8	3.7	0.016	67.4	47	0.48
RF03	29 Aug 2019	2746:33	2746:50	-13.2	11.3	4.8	0.039	47.3	1013	0.95
RF03	29 Aug 2019	2746:12	2746:27	-12.7	12.9	17.7	0.206	38.8	1393	0.97
LR06a	17 Sep 2019	0150:09	0150:50	-12.5	6.0	19.7	0.023	49.8	88	0.75
RF16	29 Sep 2019	0711:39	0712:00	-12.4	0.7	0.9	0.015	57.1	185	1.02
RF03	29 Aug 2019	2529:29	2529:32	-12.0	-999	2.0	0.025	54.1	300	1.26
LR06a	17 Sep 2019	0149:26	0149:34	-12.0	5.6	23.2	0.830	47.6	141	0.55
LR06a	17 Sep 2019	0149:51	0149:58	-12.0	3.7	14.4	0.361	39.6	316	1.17
Mean values				-13.7	5.3	8.4	0.129	52.4	323	1.08

### b. CAMP<sup>2</sup>Ex campaign

The CAMP<sup>2</sup>Ex field campaign was staged from Clark International Airport in the Philippines from 24 August to 5 October 2019. The NASA P-3B Orion and Learjet 35A research aircraft were both equipped with aerosol, air motion, and microphysical sensors. In addition the P-3B was instrumented with remote sensors and a more extensive suite of aerosol sensors. Missions were flown over the South China and Philippine Seas (here we include the Sulu Sea with the South China Sea). Nineteen missions were flown by the P-3B and 11 flown by the Learjet. Reid et al. (2021, manuscript submitted to *Bull. Amer. Meteor. Soc.*) provide a more detailed description of the CAMP2Ex project and instrumentation. A total of 1018 cloud passes were flown by the P-3 and 684 cloud passes by the Learjet. Many of the cloud passes were in alto cumulus, stratus, and scud clouds, which are eliminated from this analysis. Table 1 shows averages of microphysical parameters recorded during 116 selected cloud passes conducted by the P-3 and Learjet. The cloud penetrations were selected to represent convective updrafts that were not contaminated from sedimentation of precipitation particles. In Table 1, for a CuCg cloud pass in the “warm cloud” region or region “near 0°C” to qualify, it had to contain greater than 0.1 g m<sup>-3</sup> liquid water content (LWC) and an updraft 1 m s<sup>-1</sup> or greater anywhere within the cloud pass. In the “cloud base” region, LWC greater than 0.1 g m<sup>-3</sup> and a 1-Hz updraft greater than zero anywhere within the cloud pass were required. In the “mixed-phase” region, LWC or ice water content (IWC) greater than 0.1 g m<sup>-3</sup> and a 1-Hz updraft greater than zero anywhere within the cloud pass were required.

Table 1 is divided into four sections: cloud base with temperatures from 21.5° to 24.1°C, warm cloud with temperatures ranging from 3.1° to 21.1°C, within ±3°C of the 0°C level in ice-free updrafts, and mixed-phase from -16° to -12°C. The 39 cloud-base penetrations as measured by both aircraft had

an average drop concentration of 572 cm<sup>-3</sup> and standard deviation of 260 cm<sup>-3</sup>. The measurements of cloud-base DSDs are a proxy for boundary layer CCN (Twomey and Squires 1959; Fitzgerald 1972). The mean values in Table 1 show a decrease in drop concentration and increase in drop effective radius ( $R_{\text{eff}}$ ) with decreasing temperature, where  $R_{\text{eff}}$  is defined as the third moment of a DSD divided by its second moment. The growth in  $R_{\text{eff}}$  is in excess of expected from condensational growth (Pruppacher and Klett 1997), and suggests an active collision-coalescence process. Most of the cloud penetrations in Table 1 show values of LWC far below the adiabatic value (~6 g m<sup>-3</sup> at the 0°C level), which is suggestive of a strong entrainment-dilution process. Notable is the rapid decrease of mean LWC from the 0°C level (2.0 g m<sup>-3</sup>) to the mixed-phase region, where the mean LWC has decreased to 0.129 g m<sup>-3</sup> and IWC has increased from zero to 1.08 g m<sup>-3</sup>, suggesting a rapid freezing process. The physics behind these observations is discussed in more detail in sections 4 and 5.

Cloud-base DSDs based on combined FFSSP or FCDP and 2D-S measurements from the 39 cloud passes by the P-3 and Learjet are shown in Fig. 6a. The data in Fig. 6a show that the cloud-base DSDs were broad, extending out to between 50 and 120 μm. Figure 6b shows average DSDs from combined FFSSP or FCDP, 2D-S and HVPS measurements from 29 cloud passes within ±3°C of the 0°C level in moderate-to-strong (~5 to 15 m s<sup>-1</sup>) ice-free updrafts (Table 1). Ice-free updrafts were identified by a visual analysis of CPI and 2D-S images. The aircraft did not always fly exactly at the 0°C level, so ice-free updrafts within ±3°C were selected to increase the measurement population. The DSDs in Fig. 6b all extend past 1 mm with the majority extending past 2 mm. These data confirm that a strong collision-coalescence process was active when moderate to strong updrafts reached the 0°C level, otherwise the maximum drop diameter would not exceed about

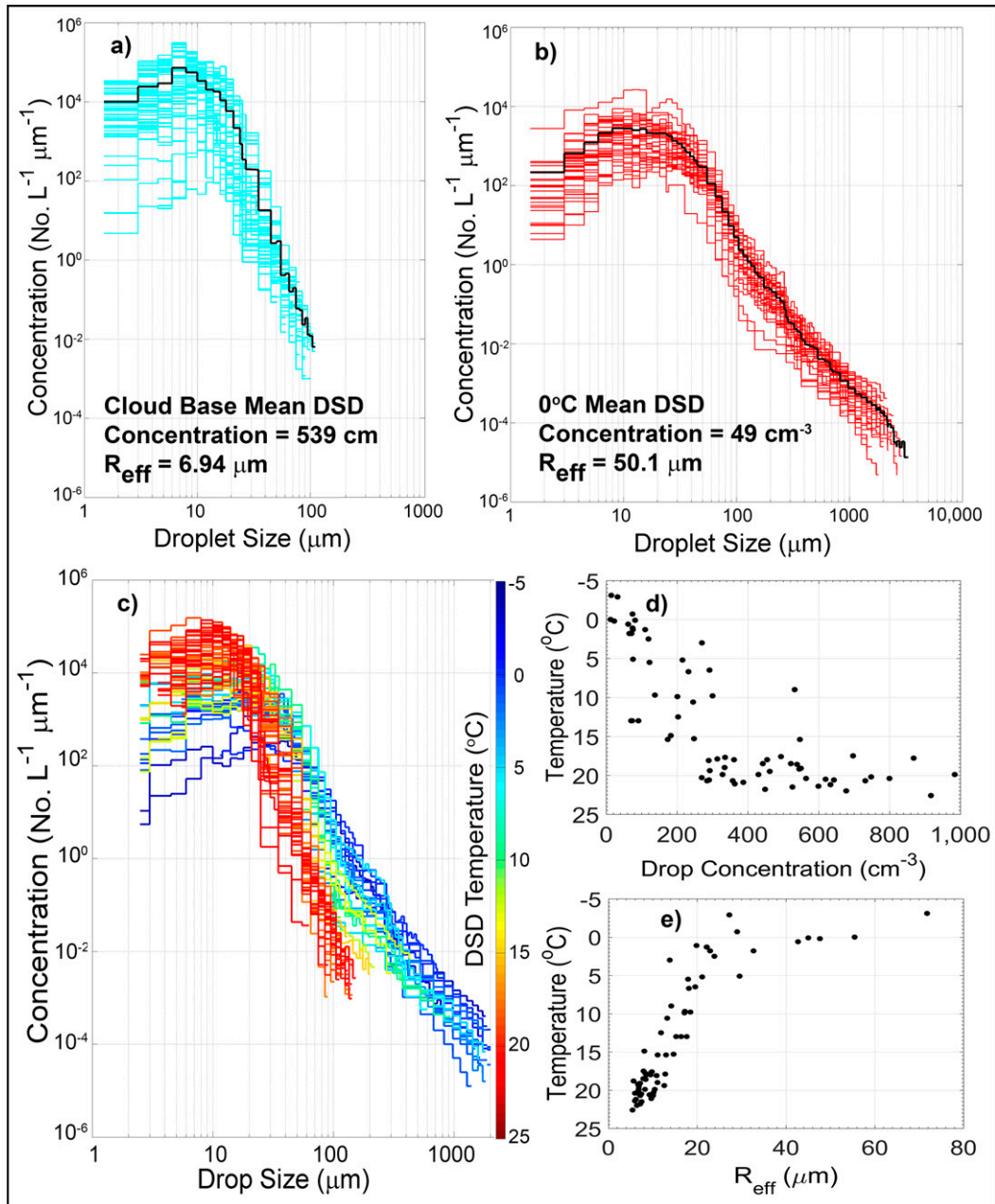


FIG. 6. DSDs sampled over the South China and Philippine Seas (a) 39 cloud penetrations within 300 m above cloud base in ice-free updrafts, (b) 29 cloud penetrations within  $\pm 3^\circ$  of the  $0^\circ\text{C}$  level, (c) plot in  $2^\circ\text{C}$  intervals from 70 cloud penetrations near cloud base to the  $-3^\circ\text{C}$  level in ice-free updrafts with a temperature scale shown at the right. (d), (e) Scatterplots of drop concentration and effective radius ( $R_{\text{eff}}$ ) vs temperature. Mean DSDs in (a) and (b) are shown by the black trace in each figure.

50- $\mu\text{m}$  diameter, as shown in High Plains CuCg by Lawson et al. (2017). Figure 6c shows a plot of DSDs as a function of temperature. The DSDs are constructed from 70 cloud passes in ice-free updrafts and averaged over  $2^\circ\text{C}$  intervals. There is a clear progression of increasing size of the largest drops and decreasing drop concentration progressing from cloud base ( $\sim 23^\circ\text{C}$ ) to the  $-3^\circ\text{C}$  level, which is expected when there is a

strong collision-coalescence process. This is also evidenced by the increased  $R_{\text{eff}}$  at the  $0^\circ\text{C}$  level ( $48.0 \mu\text{m}$ ) relative to that at cloud base ( $6.1 \mu\text{m}$ ).

The locations of cloud-base measurements in Fig. 6a are shown in Fig. 7a. Figure 7b shows locations of measurements of the concentration of drops  $\geq 300 \mu\text{m}$  within  $\pm 3^\circ\text{C}$  of the observation level in ice-free updrafts (hereafter  $N_{300}$ ), which

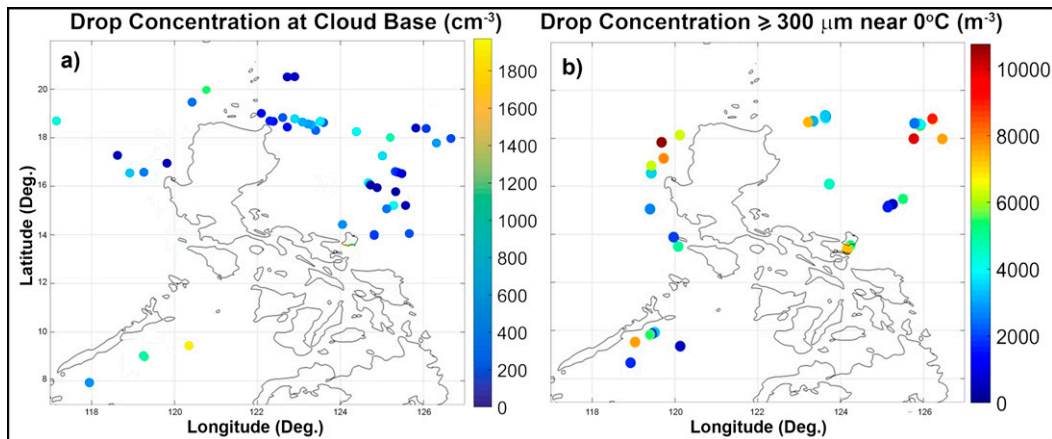


FIG. 7. Location of (a) drop concentration near cloud base and (b) drop concentration  $\geq 300 \mu\text{m}$  near the  $0^\circ\text{C}$  level ( $\pm 3^\circ\text{C}$ ). The number concentration can be estimated from the color bar at the right side of each panel.

is indicative of the strength of the coalescence process. The data points in Figs. 7a and 7b are color-coded to show the total drop concentrations at cloud base and  $N_{300}$ . The data in Figs. 6b and 7b show that the strong collision-coalescence process was active in CuCg clouds over both the South China and Philippine Seas, with no obvious correlation between the strength of coalescence and drop concentration at cloud base shown in Fig. 7a.

Figure 8a shows a time series of  $N_{300}$  where each date is a mission flown by either or both the P-3 and Learjet. Figures 8b–d show cloud-base parameters measured at the same location as  $N_{300}$ . The cloud-base drop concentrations shown in Fig. 8b range from 70 to  $1200 \text{ cm}^{-3}$ , with 80% of the measurements falling between 250 and  $1200 \text{ cm}^{-3}$  (red boxes in Fig. 8b). This reflects the polluted environment that was encountered during most of CAMP<sup>2</sup>Ex (Reid et al. 2021, manuscript submitted to *Bull. Amer. Meteor. Soc.*), with average cloud-base drop concentrations much higher than  $89 \text{ cm}^{-3}$ , the average value measured in the Caribbean (Lawson et al. 2015). The maximum size of drops measured in the average cloud-base size distribution ( $\text{DSD}_{\text{max}}$ ) is shown in Fig. 8c.  $\text{DSD}_{\text{max}}$  ranges from 50 to  $120 \mu\text{m}$  with 88% of the measurements between 60 and  $120 \mu\text{m}$  (red boxes). The relatively large values of  $\text{DSD}_{\text{max}}$  support coalescence and are similar to those found in the Caribbean (Lawson et al. 2015). Figure 8d shows relative dispersion calculations, which is the standard deviation of the average cloud-base DSD divided by its mean value. The average of all the cloud-base relative dispersion measurements, which is an indication of the breadth of the DSD, is  $0.33 \pm 0.07$ , with 84% of the measurements contained within 0.25 and 0.45 (red boxes on the plot). This suggests that the average cloud-base DSDs were relatively broad and supported the coalescence process. A comparison of the three cloud-base parameters (Figs. 8b–d) shows no obvious correlation with the formation of drops  $> 300 \mu\text{m}$  near  $0^\circ\text{C}$  in Fig. 8a; i.e., there is no obvious phase correlation in any of the cloud-base parameters with formation of large drops aloft.

#### 4. Collision-coalescence, secondary ice process, and bubble structure

##### a. Collision-coalescence

The impact that boundary layer CCN and the progression of DSDs through the warm region of cloud have on the collision-coalescence process has been studied numerically and observationally for over 60 years. The boundary layer CCN size distribution and composition are directly related to the cloud-base DSD (Twomey and Squires 1959; Fitzgerald 1972). In his review article Hudson (1993) reports that a cloud-base droplet concentration  $< 200 \text{ cm}^{-3}$  is considered maritime. The propensity for maritime convective clouds to develop a strong collision-coalescence process was described by Squires (1958). He concluded that a cloud-base drop spectrum characterized by relatively low concentration with large average and maximum droplet sizes is favorable for developing coalescence. It has also been suggested that the presence of giant and ultragiant CCN increase  $\text{DSD}_{\text{max}}$  and enhance the coalescence process (Johnson 1982).

There is a consensus in the literature that a value of  $R_{\text{eff}} > \sim 12\text{--}14 \mu\text{m}$  is indicative of an active coalescence process (Rosenfeld and Gutman 1994; Gerber 1996; Andreae et al. 2004; Freud and Rosenfeld 2012). A plot of  $R_{\text{eff}}$  as a function of height for CuCg with weak (UAE), moderate (SEUS), and strong (South China and Philippine Seas) coalescence development is shown in Fig. 9. The gray shaded area highlights the region where  $R_{\text{eff}} = 12\text{--}14 \mu\text{m}$ . The values of  $R_{\text{eff}}$  are derived from Table 1 in ice-free updrafts and support the claim that  $R_{\text{eff}} > 12\text{--}14 \mu\text{m}$  is a value where moderate to strong coalescence has developed. Note that the slope of the  $R_{\text{eff}}$  curve for South China and Philippine Seas trace becomes flatter on the right side of the gray shaded area, suggesting that the rate of collision-coalescence increases as the updraft ascends.

Freud and Rosenfeld (2012) drew on numerical simulations and limited aircraft measurements to conclude that  $R_{\text{eff}} > 14 \mu\text{m}$  is likely to result in “considerable precipitation mass” in

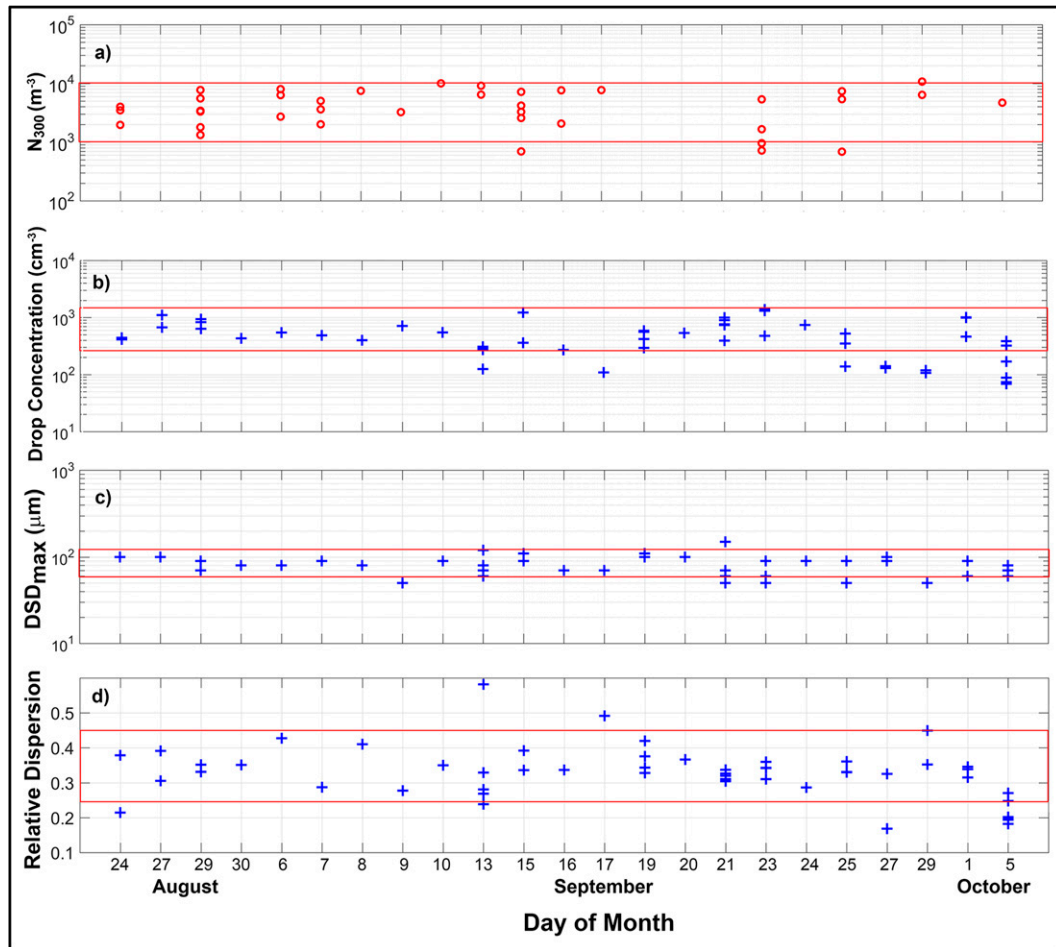


FIG. 8. (a) Time series of  $N_{300}$  within  $\pm 3^\circ\text{C}$  of the  $0^\circ\text{C}$  level, where each date is a mission flown by either or both the P-3 and Learjet. Cloud-base parameters measured at the same location as  $N_{300}$  are shown in (b) drop concentration, (c) maximum drop size ( $\text{DSD}_{\text{max}}$ ), and (d) relative dispersion. The red boxes are explained in the text.

growing convective clouds. They considered adiabatic parcels with CCN and cloud-base DSDs that did not include giant or ultragiant nuclei in their analysis. Their results suggested that, due to competition for available water vapor, high concentrations of small drops and colder cloud-base temperatures inhibited the natural increase of  $R_{\text{eff}}$  with height. It is interesting to note that they suggested their results also applied to subadiabatic updrafts, because inhomogeneous mixing did not change the shape of the DSD, only the total drop concentration.

Table 2 lists a summary of microphysical parameters from CuCg investigated at various geographical locations. Data in Table 2 represent projects in the Caribbean (ICE-T), southeast United States (SEAC<sup>4</sup>RS), the UAE (UAEREP), and South China and Philippine Seas (CAMP<sup>2</sup>Ex). The data were derived from an average of all qualifying cloud penetrations in ice-free updrafts. Data collected near Amarillo, McCook, Alliance, and Kimball, Nebraska, Pueblo, Colorado, and Cheyenne, Wyoming, in the United States are an average of all qualifying penetrations during a single mission at each

location. Table 2 is partitioned into three sections: cloud-base parameters, ice-free updraft characteristics at the observation level ( $T_{\text{OBS}}$ ), and ice formation at  $-16^\circ \leq T \leq -12^\circ\text{C}$ . Cloud-base temperature is in the first column and spans the range from  $+23^\circ\text{C}$  at the top to  $-11^\circ\text{C}$  at the bottom of the table. The regions with cloud-base temperatures  $\geq 20^\circ\text{C}$  were quasi-maritime in the SEUS, due to the advection of moisture from the Gulf of Mexico. As noted previously, the boundary layer over the UAE and South China and Philippine Seas were polluted and  $\text{DSD}_{\text{max}}$  was large in those regions. IWC values shown in the last column are determined by generating individual water and ice size distributions based on analysis of CPI, 2D-S, and HVPS images, and applying the formula from Brown and Francis (1995) to the ice size distribution. Cloud-base temperature determines the depth of warm cloud based on a lapse rate of  $2^\circ\text{C} (1000 \text{ ft})^{-1}$ . Average cloud-base drop concentrations all exceed  $245 \text{ cm}^{-3}$ , with a maximum of  $872 \text{ cm}^{-3}$ , except notably over the Caribbean, where the average cloud-base drop concentration is  $89 \text{ cm}^{-3}$  and the strongest coalescence is observed based on  $N_{300}$ .

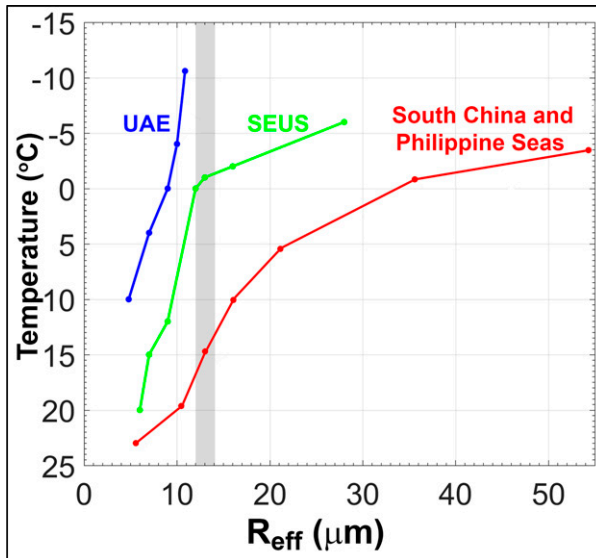


FIG. 9. Effective radius ( $R_{\text{eff}}$ ) plotted as a function of temperature in ice-free updrafts of CuCg in the United Arab Emirates (UAE), southeast United States (SEUS), and South China–Philippine Seas. The gray shaded area is the range of values where  $R_{\text{eff}}$  has been suggested as a threshold value for coalescence by Freud and Rosenfeld (2012) and others.

As noted above, several investigators have presented evidence that  $R_{\text{eff}} > \sim 12\text{--}14\ \mu\text{m}$  in convective updrafts is a good indicator of a threshold value for development of significant coalescence.  $R_{\text{eff}}$  values in ice-free updrafts at the observation level shown in Table 2 tend to support this claim. Strong to moderate coalescence is observed in CuCg where  $R_{\text{eff}}$  is significantly larger ( $22.1\text{--}62.1\ \mu\text{m}$ ) than the threshold value, and weak or no coalescence in CuCg where  $R_{\text{eff}}$  is smaller ( $5.5\text{--}11\ \mu\text{m}$ ) than the  $12\text{--}14\text{-}\mu\text{m}$  threshold value.

Another very strong indicator that coalescence will or will not develop in a moderately strong CuCg updraft is cloud-base temperature, which determines the depth of warm cloud. This can be seen in Table 2, where  $N_{300}$  increases with increasing cloud-base temperature, and also graphically in Fig. 10, which shows ice-free DSDs in CuCg updrafts from aircraft investigations in various geographical locations listed in Table 2, and examples of 2D-S images from various locations. In Fig. 10  $T_{\text{obs}}$  is the temperature at which the DSDs were sampled. The color of each DSD in Fig. 10 corresponds to its temperature at cloud base, where bluish colors are colder cloud bases and reddish colors are warmer cloud bases. The correlation between warm ( $T \geq 20^\circ\text{C}$ ) cloud-base temperatures and the development of coalescence with relatively high ( $3934\text{--}7210\ \text{m}^{-3}$ ) concentrations of drops from  $300\ \mu\text{m}$  to  $3\ \text{mm}$  is evident in Fig. 10 and Table 2. On the other hand, clouds with base temperatures  $\leq 8^\circ\text{C}$  did not develop drops larger than  $300\ \mu\text{m}$ . Clouds with base temperatures  $10^\circ \leq T \leq 14^\circ\text{C}$  developed drops from  $300\ \mu\text{m}$  to  $1\ \text{mm}$  in very low ( $30\text{--}310\ \text{m}^{-3}$ ) concentrations (Table 2).

As shown in Table 2, CuCg with the warmest average cloud-base temperatures ( $23^\circ\text{C}$ ) over tropical and subtropical

marine regions (Caribbean, South China, and Philippine Seas) develop strong coalescence.  $N_{300}$  in these regions ranges from  $4656$  to  $7210\ \text{m}^{-3}$ . CuCg in the SEUS with a cloud-base temperature of  $20^\circ\text{C}$  developed moderate coalescence with an  $N_{300}$  of  $3934\ \text{m}^{-3}$ . On the other end of the spectrum, CuCg with cloud-base temperatures ranging from  $-11^\circ$  to  $+8^\circ\text{C}$  over the High Plains (Colorado, Nebraska, and Wyoming) did not develop coalescence. In the intermediate region CuCg with cloud-base temperatures of  $14^\circ\text{C}$  (Amarillo),  $12^\circ\text{C}$  (McCook), and  $10^\circ\text{C}$  (UAE) developed weak coalescence, with  $N_{300}$  values of  $310$ ,  $120$ , and  $30\ \text{m}^{-3}$ , respectively.

The data in Table 2 are now examined to assess how the characteristics of average cloud-base DSDs affect the formation of coalescence near  $0^\circ\text{C}$ , i.e., how well the cloud-base DSDs support the premise of Squires (1958), who introduced the concept of maritime and continental DSDs (see section 4a). Inspection of all geographic locations shows that relatively low ( $89\ \text{cm}^{-3}$ ) average drop concentrations were only observed over the Caribbean. Average cloud-base drop concentrations over the South China and Philippine Seas ( $682$  and  $471\ \text{cm}^{-3}$ , respectively) were particularly high for maritime environments due to biomass burning and pollution from landmasses in Southeast Asia (Reid et al. 2021, manuscript submitted to *Bull. Amer. Meteor. Soc.*). Values of  $\text{DSD}_{\text{max}}$  were  $\geq 65\ \mu\text{m}$  in all locations except over the midlatitudes in the United States. Table 2 shows that the average cloud-base drop size was largest over the Caribbean,  $14.8\ \mu\text{m}$ , with other locations ranging from  $7.1$  to  $9.9\ \mu\text{m}$ . Thus, the generalized criteria suggested by Squires (1958) that supports the coalescence process was present only in the Caribbean. However, as we see from Fig. 10 and further inspection of Table 2, a strong coalescence process was also observed over the South China and Philippine Seas, despite the relatively high total drop concentrations at cloud base.

Total cloud-base drop concentrations over the South China and Philippine Seas are very high due to pollution, but as shown in Table 2, this did not inhibit a strong coalescence process from developing in these locations ( $N_{300} = 5457$  and  $4656$ , respectively). Measurements of mean cloud-base drop concentration over the desert region of the UAE are also very high ( $664\ \text{cm}^{-3}$ ), and  $\text{DSD}_{\text{max}}$  ( $105\ \mu\text{m}$ ) is the largest value shown in Table 2. This is explained by Wehbe et al. (2021) through a combination of sea salt from the oceans on both sides of the UAE and dust/pollution from the landmass itself. High concentrations of small cloud drops tend to inhibit condensational drop growth of the size of larger drops due to competition for water vapor. Also, Pinsky et al. (2001) show that very small cloud drops tend to be diverted around larger collector drops due to the wake created by the higher terminal velocity of the larger drop. For example, their simulations show that a  $10\text{-}\mu\text{m}$ -diameter drop has a 2% probability of colliding with a  $55\text{-}\mu\text{m}$ -diameter drop, whereas a  $20\text{-}\mu\text{m}$ -diameter drop is 15 times more likely (30% probability) of colliding with a  $55\text{-}\mu\text{m}$ -diameter drop.

Figure 11 shows a comparison of the UAE and Caribbean cloud-base DSDs. The total drop concentration in the UAE is 7 times higher and  $R_{\text{eff}}$  is about half the value of Caribbean DSD. As discussed previously, a value of  $R_{\text{eff}} = 12\text{--}14\ \mu\text{m}$  is considered a threshold for active coalescence (Freud and

TABLE 2. Data representative of 1008 aircraft penetrations of CuCg Clouds.

Location, date, No. of missions	Cloud-base characteristics					Ice-free updraft characteristics at $T_{OBS}$					Ice formation $-16^{\circ} \leq T \leq -12^{\circ}C$	
	Cloud-base $T$ ( $^{\circ}C$ )	Drop concentration ( $cm^{-3}$ )	$DSD_{max}$ ( $\mu m$ )	Mean drop size of the DSD ( $\mu m$ )	$T_{OBS}$ ( $^{\circ}C$ )	$R_{eff}$ ( $\mu m$ )	Depth of warm cloud (km)	$N_{300}$ concentration of drops $\geq 300 \mu m$ at $T_{OBS}$ ( $m^{-3}$ )	Strength of coalescence	Ice concentration ( $cm^{-3}$ )	IWC ( $g m^{-3}$ )	
Caribbean Sea, July 2011 (ICE-T), 23 missions	+23	89 $\pm$ 50	75 $\pm$ 15	14.8 $\pm$ 5.2	-7	62.1	3.51	7210 $\pm$ 3555	Strong	572	2.8	
South China Sea, Aug-Oct 2019 (CAMP <sup>2</sup> Ex), 11 missions	+23	682 $\pm$ 348	79 $\pm$ 17	8.3 $\pm$ 3.9	-5	48.1	3.51	5457 $\pm$ 2875	Strong	368	1.13	
Philippine Sea, Aug-Oct 2019 (CAMP <sup>2</sup> Ex), 18 missions	+23	471 $\pm$ 346	80 $\pm$ 23	9.9 $\pm$ 4.9	-6	52.2	3.51	4656 $\pm$ 2781	Strong	84	0.79	
Southeast United States, Aug-Sept 2013 (SEAC <sup>2</sup> RS), 7 missions	+20	689 $\pm$ 188	65 $\pm$ 16	7.8 $\pm$ 2.9	-7	28.1	3.05	3934 $\pm$ 1234	Moderate	1576	1.2	
Amarillo, 31 Jul 2017 (UAEREP)	+14	872	45	8.1 $\pm$ 2.2	-6	10.8	2.13	310	Weak	16	0.11	
McCook, 9 Aug 2017 (UAEREP)	+12	650	53	7.7 $\pm$ 2.0	-15	7.3	1.83	120	Weak	0.1	0.02	
UAE, August 2019 (UAEREP), 4 missions	+10	664 $\pm$ 139	105 $\pm$ 10	9.5 $\pm$ 2.9	-12	11.0	1.52	30 $\pm$ 13	Weak	8	0.06	
Alliance, 24 Aug 2017 (UAEREP)	+8	413	27	7.7 $\pm$ 1.9	-26	8.6	1.22	0	None	0.1	0	
Kimball, 12 Aug 2015	+2	341	25	8.8 $\pm$ 1.7	-17	5.5	0	0	None	0.04	0	
Pueblo, 14 Aug 2017	-5	494	28	7.1 $\pm$ 1.6	-16	6.1	0	0	None	0.05	0	
Cheyenne, 29 Jul 2016	-11	246	26	8.9 $\pm$ 3.7	-36	10.1	0	0	None	0.01	0	

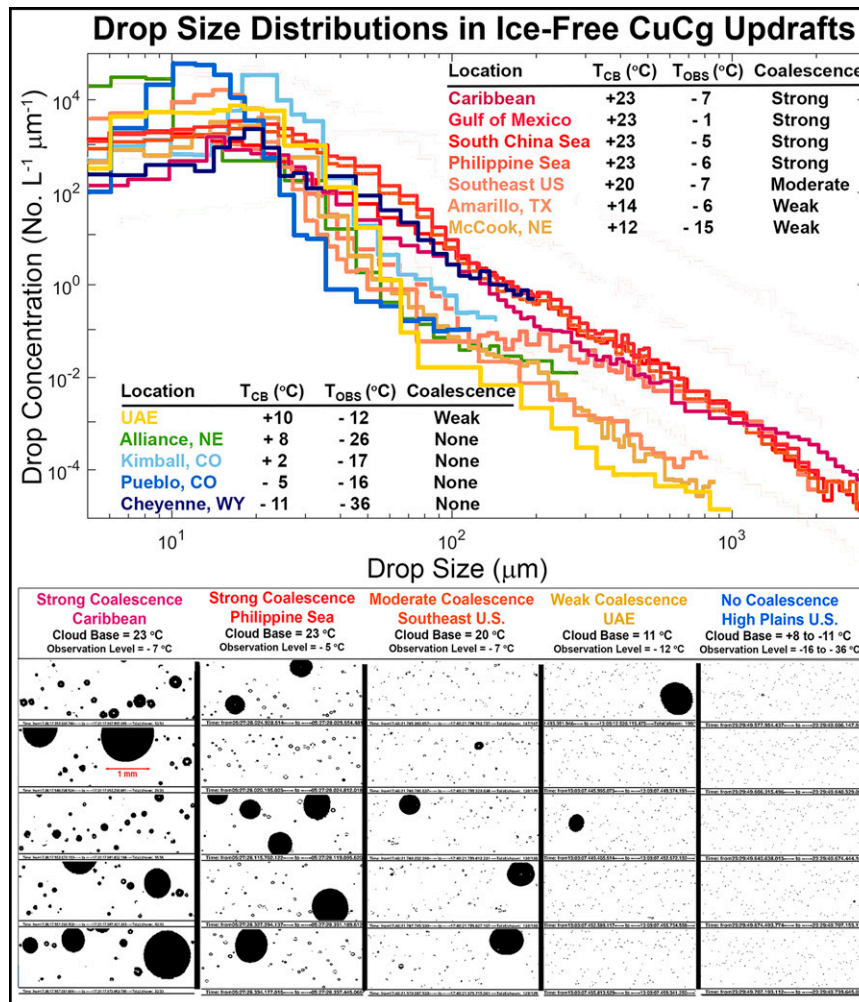


FIG. 10. (top) Average DSDs derived from data collected during penetrations by research aircraft in ice-free updraft regions of CuCg penetrated at temperature  $T_{OBS}$  with cloud-base temperature  $T_{CB}$ . The table shows the location where the data were collected with DSDs progressing from colder  $T_{CB}$  in bluish colors to warmer  $T_{CB}$  in reddish colors, which corresponds to the strength of the observed coalescence process at the  $T_{OBS}$  level. (bottom) Examples of drop images from the 10- $\mu\text{m}$  resolution 2D-S probe illustrating the development of coalescence as a function of cloud-base temperature.

Rosenfeld 2012), so the Caribbean DSD with  $R_{\text{eff}} = 9.12 \mu\text{m}$  has a considerable head start on developing strong coalescence. Also, the higher UAE concentration of drops  $< 15 \mu\text{m}$  (red shading) and lower concentration of drops from 15 to 35  $\mu\text{m}$  (gray shading) tends to inhibit drop collisions that will stimulate coalescence (Pinsky et al. 2001).

As shown in Table 2, an obvious difference in geographic regions that developed strong and moderate coalescence, compared with other regions, is the cloud-base temperature, which is reflected in the depth of warm cloud. The additional depth of warm cloud provides much more time for drop collisions and development of large drops, and may overcome the inhibiting effects that relatively high drop concentrations of small drops have on the development of coalescence. Figure 12 illustrates the significance of cloud-base temperature and

the depth of warm cloud on the development of coalescence. All of the locations with CuCg that develop moderate to strong coalescence have depths of warm cloud  $> 3 \text{ km}$ , while locations with depths of warm cloud  $< 2.13 \text{ km}$  developed weak or no coalescence. The data presented in Table 2 suggest that both the cloud-base DSD (i.e., boundary layer CCN population) and cloud-base temperature are significant factors in the development of coalescence, which is correlated with the SIP associated with drop fracturing (Fig. 1). Deconvolving these two factors may require sensitivity analyses using cloud models with sophisticated bin microphysics.

#### b. SIP

Rangno and Hobbs (1994) were first to report a quantitative correlation between drop size and the concentration of

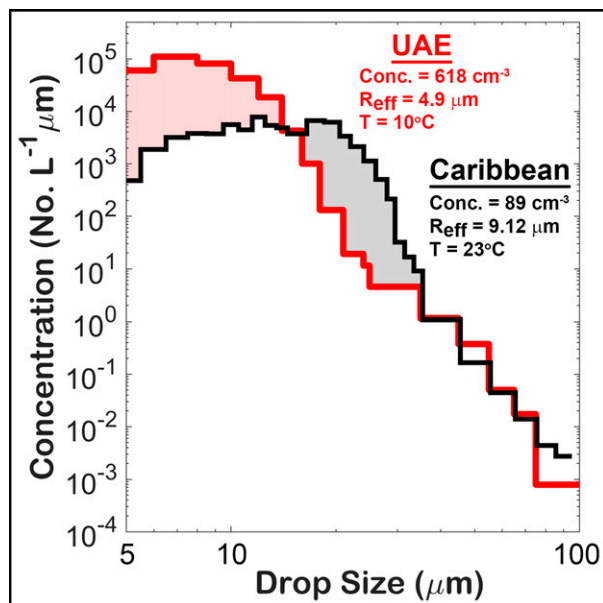


FIG. 11. Mean cloud-base DSD from the Caribbean (black) and average of the four UAE DSDs (red) shown in Fig. 4. The gray highlighted region indicates drop sizes that are conducive to collection by larger diameter drops, and the reddish region indicates drop sizes that are too small to be efficiently collected by larger drops (see text for more discussion).

IPs in midlatitude marine CuCg. Taylor et al. (2016) found a relationship between the formation of drizzle drops and high concentrations of IPs over southwest England. More recently, Luke et al. (2021) analyzed remote measurements to suggest that the formation of drizzle drops and rain in Arctic clouds is associated with rapid ice formation. As indicated by the data in Table 2 and results presented in Lawson et al. (2015, 2017), SLW in clouds that develop strong coalescence rapidly freeze and produce a SIP associated with fractured drops and spicules.

On the other hand, Table 2 shows that CuCg that did not generate high  $N_{300}$  did not produce relatively high ice particle concentrations and high IWCs in the  $-16^{\circ} \leq T \leq -12^{\circ}\text{C}$  region. The result is that small supercooled drops were carried higher in the updraft, sometimes up to the homogeneous freezing level of  $-38^{\circ}\text{C}$ . This is especially evident in the missions over the midlatitude western United States. The measurements in midlatitude western United States are not as comprehensive as those reported in other locations, largely due to the recent focus on field campaigns in tropical environments (i.e., ICE-T, SEAC<sup>4</sup>RS, and CAMP<sup>2</sup>Ex). However, there is a large dataset of measurements in the western United States from extensive legacy projects, including the National Hail Research Experiment (NHRE; 1972–76), the High Plains Cooperative Experiment (HIPLEX; 1976–80), and the Cooperative Convective Precipitation Experiment (CCOPE; 1981). Reports in the literature from this era bolster the measurements in Table 2, showing that the coalescence process was virtually absent in these midlatitude CuCg (Dye et al. 1974; Knight and Squires 1982; Cooper and Lawson

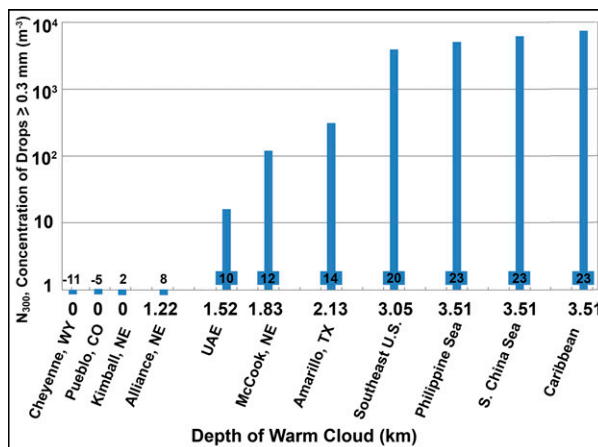


FIG. 12. Bar chart showing the relationship between  $N_{300}$ , the concentration of supercooled water drops  $\geq 0.3$  mm (i.e., strength of coalescence), as a function of the depth of warm cloud (km), based on data from the various geographical locations shown in Table 2. Numbers just above the  $x$  axis are cloud-base temperatures ( $^{\circ}\text{C}$ ).

1984; Dye et al. 1986). The exception occurs in large convective complexes and supercell storms that generate lower (warmer) cloud bases and unmixed updraft cores (Rasmussen and Heymsfield 1987; Kubesh et al. 1988).

In the 1970s and 1980s NCAR operated an instrumented sailplane (i.e., glider) during the NHRE and CCOPE projects in eastern Colorado and southeastern Montana. During its ascents in updrafts, the sailplane provides a unique, quasi-Lagrangian view of ice evolution that is not practical with powered aircraft. The instrumented sailplane was equipped with a custom cloud particle camera that showed a distinctive absence of large drops indicating a lack of coalescence (Dye et al. 1974, 1986; Heymsfield et al. 1978, 1979). An example of a continuous sailplane ascent in an updraft with an unmixed core from cloud base at  $2.5^{\circ}$  to  $-21^{\circ}\text{C}$  showed that the first IPs did not form until about the  $-18^{\circ}\text{C}$  level (Dye et al. 1986). This is in striking contrast to CuCg with warm ( $\geq 20^{\circ}\text{C}$ ) cloud-base temperatures and broad DSDs, where ice forms after development of SLDs and the updraft is mostly frozen by the  $-16^{\circ}\text{C}$  level (Lawson et al. 2015, 2017).

Table 2 shows  $N_{300}$  versus ice particle concentration and Fig. 13 shows a plot of  $N_{300}$  versus IWC in updrafts at  $-16^{\circ} \leq T \leq -12^{\circ}\text{C}$  for the geographic locations shown in Table 2. The IWC was computed by applying the formula from Brown and Francis (1995). The rapid freezing of drops in the  $-16^{\circ} \leq T \leq -12^{\circ}\text{C}$  region, which is indicated by high ( $84\text{--}1576\text{ L}^{-1}$ ) ice particle concentrations in Table 2, far exceeds the concentration of INPs ( $\sim 10^{-3}\text{--}10^{-4}$ ) at that range of temperatures (DeMott et al. 2016). The strong coalescence associated with high ice particle concentrations is indicative of an active SIP in CuCg. Lawson et al. (2015, 2017) provide compelling evidence that the SIP observed in CuCg associated with a strong coalescence process is the result of fracturing and spicule formation in SLDs (Fig. 1). Figure 13 strengthens this argument

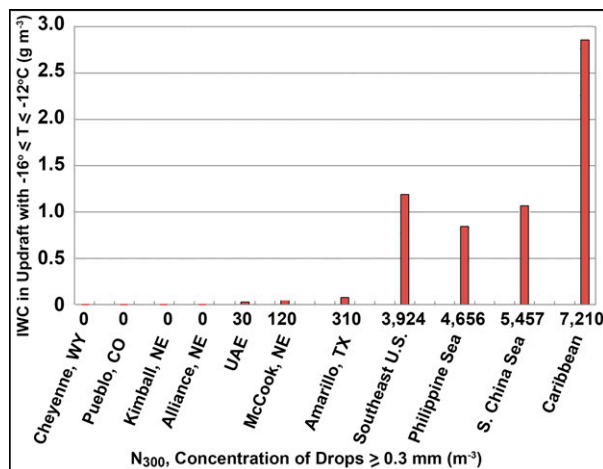


FIG. 13. Bar chart showing the relationship between ice water content (IWC) for  $-16^\circ \leq T \leq -12^\circ\text{C}$  as a function of  $N_{300}$ , the concentration of supercooled water drops  $\geq 0.3$  mm, based on data from the various geographical locations shown in Table 2.

showing the relationship between the strength of coalescence (i.e.,  $N_{300}$ ) and IWC in the  $-16^\circ \leq T \leq -12^\circ\text{C}$  region.

### c. Bubble structure of CuCg

Observations and numerical models indicate that CuCg clouds consist of a series of buoyant “bubbles” that start at cloud base and terminate near cloud top unless entrainment of environmental air results in negative buoyancy lower in the cloud. Scorer and Ludlam (1953) introduced a conceptual model of a thermally buoyant bubble that rises while the air above is lifted and drains down the outside. More recent high-resolution numerical simulations reveal a toroidal circulation with an updraft in the core of a thermal bubble and downdrafts at the edges (Moser and Lasher-Trapp 2017; Morrison et al. 2020). Downdrafts at the edges of updrafts in CuCg are often identified from aircraft data and transport ice particles downward from colder temperatures aloft (Heymsfield et al. 1979; Blyth et al. 1988; Blyth and Latham 1993).

Heymsfield et al. (1978, 1979) drew conclusions from 12 sailplane ascents in CuCg during the NHRE project. The sailplane has a descent rate of about  $1 \text{ m s}^{-1}$ , so it was able to climb within an ascending bubble that had a mean updraft velocity larger than its sink rate. The mean updraft velocity at cloud base for the sailplane ascents was  $4.1 \text{ m s}^{-1}$  and generally increased with altitude (Heymsfield et al. 1978). The authors concluded that air rises adiabatically in the updrafts of High Plains CuCg with primary nucleation being responsible for production of the first IPs. They hypothesize that large IPs in downdrafts at the edges of the updraft are responsible for their observations of IPs at temperatures warmer than possible from primary nucleation. Observations from the sailplane orbiting in the updraft showed that IPs tend to mix inward from the downdrafts toward the center of the updraft.

Learjet observations of CuCg during the CAMP<sup>2</sup>Ex project over the South China and Philippine Seas also displayed a bubble-like morphology with IPs descending at the edges of

updrafts. Figure 14 shows an example of data collected in a mixed-phase turret at  $-7.9^\circ\text{C}$ . Figure 14a shows a time series of updraft velocity and LWC indicating a downdraft with a maximum of  $-4.8 \text{ m s}^{-1}$  from 0720:01 to 0720:06 UTC, followed by an updraft with a peak of  $7.4 \text{ m s}^{-1}$  at 0720:13 UTC. Figures 14b and 14c show examples of particle images and Fig. 14d shows supercooled DSDs (blue) and ice PSDs (red) that have been separated using CPI and 2D-S particle imagery. The images and size distributions have been arranged from left to right in Fig. 14d so that they roughly correspond with the location of the downdraft at edge of the updraft (bubble) and the peak velocity in the middle of the updraft. There is a clear trend in the images (Figs. 14b,c) showing that (nonspherical) IPs are found in the moist downdraft at the edge of the bubble, and their number decreases with distance toward the center of the updraft, where there are no IPs. This corresponds with the increase of IPs in the large tail of the ice size distributions shown in Fig. 14d. This example is representative of cloud penetrations that exhibit this trend in CuCg in all geographical locations.

## 5. Summary and discussion

The data presented here in Table 2 and Fig. 12 show that CuCg over open oceans with cloud-base temperatures  $\geq 23^\circ\text{C}$  (Caribbean, South China, and Philippine Seas) always develop a strong collision–coalescence process, forming relatively high concentrations of supercooled large drops (SLDs) and frozen fractured drops that are associated with a secondary ice process (SIP), resulting in rapid freezing of supercooled liquid water (SLW) in the updraft. CuCg over land near the Gulf of Mexico (SEUS in Table 2) with cloud-base temperatures  $\sim 20^\circ\text{C}$  experienced moderate coalescence. CuCg over semi-arid and arid regions in the UAE and west Texas with cloud-base temperatures  $10^\circ \leq T \leq 14^\circ\text{C}$  developed weak coalescence. CuCg over the High Plains in the United States with cloud-base temperatures  $\leq 8^\circ\text{C}$  did not develop detectable coalescence. SLW was transported to higher (colder) regions in the cloud in the locations with weak or no coalescence. The development of coalescence was also found to be correlated with a value of  $R_{\text{eff}} > \sim 12\text{--}14 \mu\text{m}$  in updrafts in the warm portion of CuCg, which is in agreement with results shown in Freud and Rosenfeld (2012).

Figure 13 shows a relationship between the strength of the coalescence process and the development of ice particles (IPs) in the region from  $-16^\circ \leq T \leq -12^\circ\text{C}$ , indicating that SLW rapidly freezes in updrafts that form a moderate to strong coalescence process. On the other hand, CuCg that do not develop coalescence loft SLW in small cloud drops to much higher elevations, occasionally to the homogeneous freezing level of  $-38^\circ\text{C}$  (Rosenfeld and Woodley 2000; Lawson et al. 2017). The correlation between the formation of SLDs and the production of IPs (Table 2 and Fig. 13) provides strong evidence that the fundamental process responsible for rapid freezing of SLW in association with coalescence is a SIP. Analysis of CPI and 2D-S images shows that the temperature region where SLDs freeze is strongly associated with images of frozen fractured drops and frozen drops with spicules (see examples in Lawson et al. 2015). The trigger for the

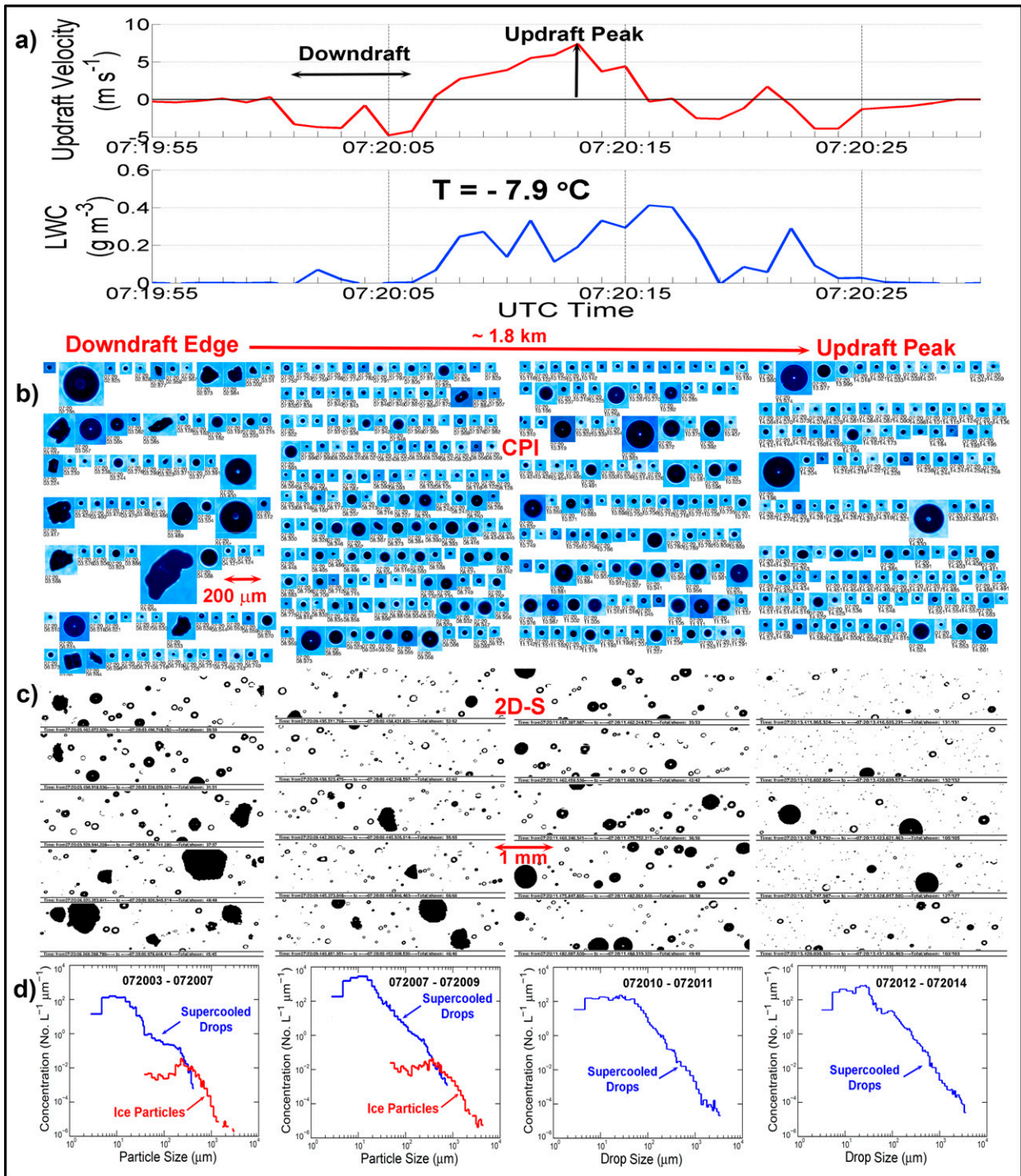


FIG. 14. (a) Time series of updraft velocity and liquid water content (LWC), showing a left-to-right transition from downdraft to updraft, (b) CPI 2.3- $\mu\text{m}$  resolution, and (c) 2D-S 10- $\mu\text{m}$  resolution particle images, and (d) PSDs separated into water and ice components. Data collected in a CuCg on 25 Sep 2019 over the Philippine Sea suggesting progression of ice particles in a downdraft mixing into an updraft.

SIP appears to be rare nucleation events at  $-6 \leq T \leq -12^\circ\text{C}$ , followed by SLD fracturing and spicule formation that produce small IPs throughout the supercooled updraft. The differential in fall velocities between the small IPs and SLDs

facilitates IP-SLD collisions, resulting in an avalanche drop-freezing process (Fig. 1).

A bubble-like morphology with downdrafts at the edges of an updraft is observed in all CuCg, except in protected

updrafts found in larger multicell systems and supercells. In CuCg with cloud-base temperatures  $\geq \sim 20^\circ\text{C}$  SLDs freeze at relatively warm ( $\sim -12^\circ$  to  $-16^\circ\text{C}$ ) temperatures due to the SIP associated with coalescence, drop fracturing, and spicule production. In CuCg over the High Plains with cloud-base temperatures  $\leq \sim 8^\circ\text{C}$ , SLW is lofted in small drops to much colder temperatures. The rapid freezing process associated with the SIP in warmer-based CuCg depletes SLW quickly in the  $-12^\circ$  to  $-16^\circ\text{C}$  temperature range. On the other hand, SLW lofted to colder temperatures in CuCg with cloud-base temperatures  $\leq \sim 8^\circ\text{C}$  offers an opportunity for recirculation in downdrafts to play a larger role in freezing SLW at warmer temperatures. Heymsfield et al. (1979) reached a similar conclusion based on data collected from sailplane ascents in CuCg in northeastern Colorado. The authors compared INP and IP measurements in adiabatic updrafts and concluded that primary nucleation was responsible for the initiation of IPs. They also suggested that recirculation of large IPs from colder temperatures was the primary precipitation mechanism.

The bubble-recirculation concept also supports a scenario where graupel particles can be recirculated into the temperature range ( $-3^\circ \leq T \leq -8^\circ\text{C}$ ) where the Hallett–Mossop (H-M) SIP is active (Hallett and Mossop 1974). The scenario of successive bubbles with downdrafts at the edges of an updraft is consistent with observations presented by Lasher-Trapp et al. (2016) and Heymsfield and Willis (2014). Lasher-Trapp et al. (2016) found that graupel particles were ascending/descending into, or balanced within, the H-M temperature region in ICE-T clouds. They concluded that the observations alone were insufficient to test if H-M SIP could explain the observed graupel increases at  $-3^\circ \leq T \leq -8^\circ\text{C}$  because of the dynamical complexity and related size sorting. Using a statistical approach, Heymsfield and Willis (2014) found that anomalously high concentrations of IPs in the H-M temperature region were correlated with low ( $\pm 1 \text{ m s}^{-1}$ ) updraft velocities and low ( $\sim 0.1 \text{ g m}^{-3}$ ) LWCs. The measurements presented in Lawson et al. (2015) focused on new, growing turrets with a mean updraft velocity of  $9.5 \text{ m s}^{-1}$  and mean LWC of  $3.5 \text{ g m}^{-3}$  in the H-M temperature zone, which was devoid of IPs. They also concluded that, based on H-M SIP rates by Mossop (1985) and Rangno and Hobbs (1991), the H-M process would take far too long to produce the observed concentrations of IPs in these strong updrafts. The measurements presented in this paper followed the same observation protocols as described in Lawson et al. (2015), which argue against the H-M process contributing to anomalously high IP concentrations in fresh, growing turrets; the exception to this conclusion is in quiescent (decaying) clouds and where recirculation of IPs is a factor.

The data in Table 2 and Figs. 12 and 13 suggest a strong relationship between cloud-base temperature and the elevation where SLW is depleted in CuCg. However, it is not clear how contributory the cloud-base DSD (i.e., boundary layer CCN population) is in development of coalescence and the associated SIP. The measurements from CAMP<sup>2</sup>Ex (South China and Philippine Seas) show that a strong coalescence process occurs even when cloud-base DSDs are well in excess

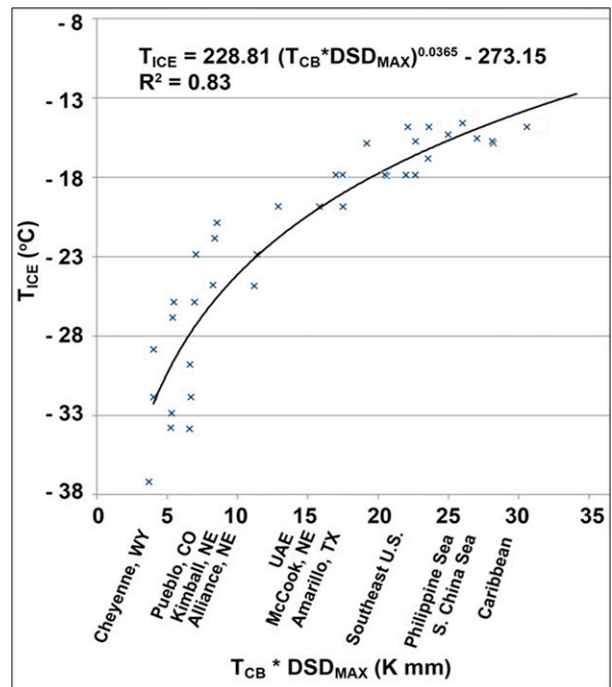


FIG. 15. Temperature ( $T_{ICE}$ ) where approximately 90% of the adiabatic liquid water content has depleted, plotted against the product of cloud-base temperature ( $T_{CB}$ ) times the maximum drop size ( $DSD_{max}$ ) measured at cloud base. The geographic locations represent locations where the CuCg were sampled. Best-fit power law and correlation coefficient are shown on the plot.

of  $400 \text{ cm}^{-3}$  (Table 2). On the other hand, cloud-base DSDs in the UAE are very broad, extending out to an average of  $105 \mu\text{m}$ , yet the coalescence process is very weak and there is no evidence of a SIP. A comparison of cloud-base DSDs from the Caribbean and UAE (Fig. 11) suggests that a relatively high concentration of drops in the  $15\text{--}35\text{-}\mu\text{m}$  size range may enhance coalescence, whereas smaller drops may inhibit coalescence. This is because the drops in the  $15\text{--}35\text{-}\mu\text{m}$  size range have an order of magnitude larger collision efficiency with drops  $> 55 \mu\text{m}$ .

Wherever available, measurements of the maximum elevation of SLW were collected from the Nevzorov hot-wire LWC probe, and if drops larger than about  $50 \mu\text{m}$  were present, by integrating the liquid DSD from imaging probes. Measurements of the maximum elevations of SLW were not always possible due to limitations imposed by air traffic control, or because the clouds developed into larger systems that were hazardous to flight. Based on available measurements, Fig. 15 shows a relationship between the product of the average cloud-base temperature,  $T_{CB}$  (K), times  $DSD_{max}$  (mm), and  $T_{ICE}$  ( $^\circ\text{C}$ ), the temperature level where approximately 90% of the adiabatic SLW is consumed, or the updraft reached the homogeneous freezing level ( $-38^\circ\text{C}$ ). The measurements are also identified by the various geographical locations identified in Table 2. Figure 15 shows a distinct trend indicating that the product of cloud-base temperature and  $DSD_{max}$  are strongly

correlated with the maximum elevation of SLW. The best-fit equation in Fig. 15 can be used as a check on cloud-resolving models that include a coalescence process and a SIP. Larger-scale models, such as climate prediction models, may be able to use the results in the parameterization of vertical transport of SLW in convection schemes.

*Acknowledgments.* This research was supported by the National Aeronautics and Space Administration Grants NNX12AC14G (SEAC<sup>4</sup>RS) and 80NSSC18K0143 (CAMP<sup>2</sup>Ex); the National Science Foundation Grant AGS-1064144 (ICE-T); and the National Center of Meteorology, Abu Dhabi, UAE, under the UAE Research Program for Rain Enhancement Science. The authors are indebted to the pilots, support crews, scientists, and graduate students who participated in the field campaigns. The National Center for Atmospheric Research is sponsored by the National Science Foundation.

*Data availability statement.* Data are available at the following locations: SPEC Learjet and NCAR C-130 ICE-T: [https://data.eol.ucar.edu/master\\_lists/generated/ice-t/](https://data.eol.ucar.edu/master_lists/generated/ice-t/); SPEC Learjet and NASA DC-8 SEAC<sup>4</sup>RS: <https://www-air.larc.nasa.gov/cgi-bin/ArcView/seac4rs>; SPEC Learjet and NASA P-3B CAMP<sup>2</sup>Ex: <https://www-air.larc.nasa.gov/cgi-bin/ArcView/camp2ex>; SPEC Learjet UAEREP in the UAE 2019: <https://eft.ncms.ae>; SPEC Learjet in the United States 2015–17: [www.specinc.com/contact](http://www.specinc.com/contact).

## REFERENCES

- Andreae, M. D., and Coauthors, 2004: Smoking rain clouds over the Amazon. *Science*, **303**, 1337–1342, <https://doi.org/10.1126/science.1092779>.
- Beswick, K. M., M. W. Gallagher, A. R. Webb, E. G. Norton, and F. Perry, 2008: Application of the Aventech AIMMS20AQ airborne probe for turbulence measurements during the Convective Storm Initiation Project. *Atmos. Chem. Phys.*, **8**, 5449–5463, <https://doi.org/10.5194/acp-8-5449-2008>.
- Bigg, E. K., 1973: Ice nucleus concentrations in remote areas. *J. Atmos. Sci.*, **30**, 1153–1157, [https://doi.org/10.1175/1520-0469\(1973\)030<1153:INCIRA>2.0.CO;2](https://doi.org/10.1175/1520-0469(1973)030<1153:INCIRA>2.0.CO;2).
- Blyth, A. M., and J. Latham, 1993: Development of ice and precipitation in New Mexican summertime cumulus clouds. *Quart. J. Roy. Meteor. Soc.*, **119**, 91–120, <https://doi.org/10.1002/qj.49711950905>.
- , W. A. Cooper, and J. B. Jensen, 1988: A study of the source of entrained air in Montana cumuli. *J. Atmos. Sci.*, **45**, 3944–3964, [https://doi.org/10.1175/1520-0469\(1988\)045<3944:ASOTSO>2.0.CO;2](https://doi.org/10.1175/1520-0469(1988)045<3944:ASOTSO>2.0.CO;2).
- Brown, P. R. A., and P. N. Francis, 1995: Improved measurements of the ice water content in cirrus using a total-water probe. *J. Atmos. Oceanic Technol.*, **12**, 410–414, [https://doi.org/10.1175/1520-0426\(1995\)012<0410:IMOTIW>2.0.CO;2](https://doi.org/10.1175/1520-0426(1995)012<0410:IMOTIW>2.0.CO;2).
- Cai, Y., J. R. Snider, and P. Wechsler, 2013: Calibration of the passive cavity aerosol spectrometer probe for airborne determination of the size distribution. *Atmos. Meas. Tech.*, **6**, 2349–2358, <https://doi.org/10.5194/amt-6-2349-2013>.
- Cooper, W. A., and R. P. Lawson, 1984: Physical interpretation of results from the HIPLEX-1 experiment. *J. Appl. Meteor.*, **23**, 523–540, [https://doi.org/10.1175/1520-0450\(1984\)023<0523:PIORFT>2.0.CO;2](https://doi.org/10.1175/1520-0450(1984)023<0523:PIORFT>2.0.CO;2).
- DeMott, P. J., and Coauthors, 2016: Sea spray aerosol as a unique source of ice nucleating particles. *Proc. Natl. Acad. Sci. USA*, **113**, 5797–5803, <https://doi.org/10.1073/pnas.1514034112>.
- Dye, J. E., C. A. Knight, V. Tootenhoofd, and T. W. Cannon, 1974: The mechanism of precipitation formation in northeastern Colorado cumulus III. Coordinated microphysical and radar observations and summary. *J. Atmos. Sci.*, **31**, 2152–2159, [https://doi.org/10.1175/1520-0469\(1974\)031<2152:TMOPFI>2.0.CO;2](https://doi.org/10.1175/1520-0469(1974)031<2152:TMOPFI>2.0.CO;2).
- , and Coauthors, 1986: Early electrification and precipitation development in a small, isolated Montana cumulonimbus. *J. Geophys. Res.*, **91**, 1231–1247, <https://doi.org/10.1029/JD091iD01p01231>.
- Fitzgerald, J. W., 1972: A study of the initial phase of cloud droplet growth by condensation. Ph.D. thesis, University of Chicago, 144 pp.
- Freud, E., and D. Rosenfeld, 2012: Linear relation between convective cloud drop number concentration and depth for rain initiation. *J. Geophys. Res.*, **117**, D02207, <https://doi.org/10.1029/2011JD016457>.
- Gerber, H., 1996: Microphysics of marine stratocumulus clouds with two drizzle modes. *J. Atmos. Sci.*, **53**, 1649–1662, [https://doi.org/10.1175/1520-0469\(1996\)053<1649:MOMSCW>2.0.CO;2](https://doi.org/10.1175/1520-0469(1996)053<1649:MOMSCW>2.0.CO;2).
- Hallett, J., and S. C. Mossop, 1974: Production of secondary ice particles during the riming process. *Nature*, **249**, 26–28, <https://doi.org/10.1038/249026a0>.
- Heymsfield, A. J., and P. Willis, 2014: Cloud conditions favoring secondary ice particle production in tropical maritime convection. *J. Atmos. Sci.*, **71**, 4500–4526, <https://doi.org/10.1175/JAS-D-14-0093.1>.
- , P. N. Johnson, and J. E. Dye, 1978: Observations of moist adiabatic ascent in northeast Colorado cumulus congestus clouds. *J. Atmos. Sci.*, **35**, 1689–1703, [https://doi.org/10.1175/1520-0469\(1978\)035<1689:OOMAAI>2.0.CO;2](https://doi.org/10.1175/1520-0469(1978)035<1689:OOMAAI>2.0.CO;2).
- , C. A. Knight, and J. E. Dye, 1979: Ice initiation in unmixed updraft cores in northeastern Colorado cumulus congestus clouds. *J. Atmos. Sci.*, **36**, 2216–2229, [https://doi.org/10.1175/1520-0469\(1979\)036<2216:IIUUC>2.0.CO;2](https://doi.org/10.1175/1520-0469(1979)036<2216:IIUUC>2.0.CO;2).
- Hudson, J. G., 1993: Cloud condensation nuclei. *J. Appl. Meteor.*, **32**, 596–607, [https://doi.org/10.1175/1520-0450\(1993\)032<0596:CCN>2.0.CO;2](https://doi.org/10.1175/1520-0450(1993)032<0596:CCN>2.0.CO;2).
- Johnson, D. B., 1982: The role of giant and ultragiant aerosol particles in warm rain initiation. *J. Atmos. Sci.*, **39**, 448–460, [https://doi.org/10.1175/1520-0469\(1982\)039<0448:TROGAU>2.0.CO;2](https://doi.org/10.1175/1520-0469(1982)039<0448:TROGAU>2.0.CO;2).
- Johnson, R. H., T. M. Rickenbach, S. A. Rutledge, P. E. Ciesielski, and W. H. Schubert, 1999: Trimodal characteristics of tropical convection. *J. Climate*, **12**, 2397–2418, [https://doi.org/10.1175/1520-0442\(1999\)012<2397:TCOTC>2.0.CO;2](https://doi.org/10.1175/1520-0442(1999)012<2397:TCOTC>2.0.CO;2).
- Keinert, A., D. Spannagel, T. Leisner, and A. Kiselev, 2020: Secondary ice production upon freezing of freely falling drizzle droplets. *J. Atmos. Sci.*, **77**, 2959–2967, <https://doi.org/10.1175/JAS-D-20-0081.1>.
- Knight, C. A., and P. Squires, 1982: *Hailstorms of the Central High Plains*. Vol. 1. University Press of Colorado, 282 pp.
- Koenig, L. R., 1963: The glaciating behavior of small cumulonimbus clouds. *J. Atmos. Sci.*, **20**, 29–47, [https://doi.org/10.1175/1520-0469\(1963\)020<0029:TGBOSC>2.0.CO;2](https://doi.org/10.1175/1520-0469(1963)020<0029:TGBOSC>2.0.CO;2).

- , 1965: Drop freezing through drop breakup. *J. Atmos. Sci.*, **22**, 448–451, [https://doi.org/10.1175/1520-0469\(1965\)022<0448:DFTDB>2.0.CO;2](https://doi.org/10.1175/1520-0469(1965)022<0448:DFTDB>2.0.CO;2).
- Korolev, A. V., and T. Leisner, 2020: Review of experimental studies of secondary ice production. *Atmos. Chem. Phys.*, **20**, 11 767–11 797, <https://doi.org/10.5194/acp-20-11767-2020>.
- , J. W. Strapp, G. A. Isaac, and A. N. Nevzorov, 1998: The Nevzorov airborne hot-wire LWC–TWC probe: Principle of operation and performance characteristics. *J. Atmos. Oceanic Technol.*, **15**, 1495–1510, [https://doi.org/10.1175/1520-0426\(1998\)015<1495:TNAHWL>2.0.CO;2](https://doi.org/10.1175/1520-0426(1998)015<1495:TNAHWL>2.0.CO;2).
- Kubesh, R. S., D. J. Musil, R. D. Farley, and H. D. Orville, 1988: The 1 August 1981 CCOPE storm: Observations and modeling results. *J. Meteor. Climatol.*, **27**, 216–243, [https://doi.org/10.1175/1520-0450\(1988\)027<0216:TAMSOA>2.0.CO;2](https://doi.org/10.1175/1520-0450(1988)027<0216:TAMSOA>2.0.CO;2).
- Lasher-Trapp, S., and Coauthors, 2016: A multisensor investigation of rime splintering in tropical maritime cumuli. *J. Atmos. Sci.*, **73**, 2547–2564, <https://doi.org/10.1175/JAS-D-15-0285.1>.
- Lauber, A., A. Kiselev, T. Pander, P. Handmann, and T. Leisner, 2018: Secondary ice formation during freezing of levitated droplets. *J. Atmos. Sci.*, **75**, 2815–2826, <https://doi.org/10.1175/JAS-D-18-0052.1>.
- Lawson, R. P., R. E. Stewart, and L. J. Angus, 1998: Observations and numerical simulations of the origin and development of very large snowflakes. *J. Atmos. Sci.*, **55**, 3209–3229, [https://doi.org/10.1175/1520-0469\(1998\)055<3209:OANSOT>2.0.CO;2](https://doi.org/10.1175/1520-0469(1998)055<3209:OANSOT>2.0.CO;2).
- , B. A. Baker, C. G. Schmitt, and T. L. Jensen, 2001: An overview of microphysical properties of Arctic clouds observed in May and July during FIRE ACE. *J. Geophys. Res.*, **106**, 14 989–15 014, <https://doi.org/10.1029/2000JD900789>.
- , and Coauthors, 2006: The 2D-S (stereo) probe: Design and preliminary tests of a new airborne, high speed, high-resolution particle imaging probe. *J. Atmos. Oceanic Technol.*, **23**, 1462–1477, <https://doi.org/10.1175/JTECH1927.1>.
- , S. Woods, and H. Morrison, 2015: The microphysics of ice and precipitation development in tropical cumulus clouds. *J. Atmos. Sci.*, **72**, 2429–2445, <https://doi.org/10.1175/JAS-D-14-0274.1>.
- , C. Gurganus, S. Woods, and R. Brientjes, 2017: Aircraft observations of cumulus microphysics ranging from the tropics to midlatitudes: Implications for a “new” secondary ice process. *J. Atmos. Sci.*, **74**, 2899–2920, <https://doi.org/10.1175/JAS-D-17-0033.1>.
- Luke, E. P., F. Yang, P. Kollilas, A. M. Vogelmann, and M. Maahn, 2021: New insights into ice multiplication using remote-sensing observations of slightly supercooled mixed-phase clouds in the Arctic. *Proc. Natl. Acad. Sci. USA*, **118**, e2021387118, <https://doi.org/10.1073/pnas.2021387118>.
- Morrison, H., J. M. Peters, A. C. Varble, W. M. Hannah, and S. E. Giangrande, 2020: Thermal chains and entrainment in cumulus updrafts. Part I: Theoretical description. *J. Atmos. Sci.*, **77**, 3637–3660, <https://doi.org/10.1175/JAS-D-19-0243.1>.
- Moser, D. H., and S. Lasher-Trapp, 2017: The influence of successive thermals on entrainment and dilution in a simulated cumulus congestus. *J. Atmos. Sci.*, **74**, 375–392, <https://doi.org/10.1175/JAS-D-16-0144.1>.
- Mossop, S. C., 1985: The microphysical properties of supercooled cumulus clouds in which an ice particle multiplication process operated. *Quart. J. Roy. Meteor. Soc.*, **111**, 183–198, <https://doi.org/10.1256/smsqj.46707>.
- O'Connor, D., B. Baker, and R. P. Lawson, 2008: Upgrades to the FSSP-100 electronics. *Int. Conf. on Clouds and Precipitation*, Cancun, Mexico, IAMAS, [http://cabernet.atmosfcu.unam.mx/ICCP-2008/abstracts/Program\\_on\\_line/Poster\\_13/O-Connor\\_extended.pdf](http://cabernet.atmosfcu.unam.mx/ICCP-2008/abstracts/Program_on_line/Poster_13/O-Connor_extended.pdf).
- Pinsky, M., A. Khain, and M. Shapiro, 2001: Collision efficiency of drops in a wide range of Reynolds numbers: Effects of pressure on spectrum evolution. *J. Atmos. Sci.*, **58**, 742–764, [https://doi.org/10.1175/1520-0469\(2001\)058<0742:CEODIA>2.0.CO;2](https://doi.org/10.1175/1520-0469(2001)058<0742:CEODIA>2.0.CO;2).
- Pruppacher, H. R., and J. D. Klett, 1997: *Microphysics of Clouds and Precipitation*. Kluwer Academic, 954 pp.
- Rangno, A. L., and P. V. Hobbs, 1991: Ice particle concentrations and precipitation development in small polar maritime cumuliform clouds. *Quart. J. Roy. Meteor. Soc.*, **117**, 207–241, <https://doi.org/10.1002/qj.49711749710>.
- , and —, 1994: Ice particle concentrations and precipitation development in small continental cumuliform clouds. *Quart. J. Roy. Meteor. Soc.*, **120**, 573–601, <https://doi.org/10.1002/qj.49712051705>.
- Rasmussen, R. M., and A. J. Heymsfield, 1987: Melting and shedding of graupel and hail: Part III: Investigations of the role of shed drops as hail embryos in the 1 August CCOPE severe storm. *J. Atmos. Sci.*, **44**, 2783–2803, [https://doi.org/10.1175/1520-0469\(1987\)044<2783:MASOGA>2.0.CO;2](https://doi.org/10.1175/1520-0469(1987)044<2783:MASOGA>2.0.CO;2).
- Rosenfeld, D., and G. Gutman, 1994: Retrieving microphysical properties near the tops of potential rain clouds by multispectral analysis of AVHRR data. *Atmos. Res.*, **34**, 259–283, [https://doi.org/10.1016/0169-8095\(94\)90096-5](https://doi.org/10.1016/0169-8095(94)90096-5).
- , and W. L. Woodley, 2000: Deep convective clouds with sustained supercooled liquid water down to  $-37.5^{\circ}\text{C}$ . *Nature*, **405**, 440–442, <https://doi.org/10.1038/35013030>.
- Scorer, R. S., and F. H. Ludlam, 1953: Bubble theory of penetrative convection. *Quart. J. Roy. Meteor. Soc.*, **79**, 94–103, <https://doi.org/10.1002/qj.49707933908>.
- Semeniuk, T. A., R. T. Brientjes, V. Salazar, D. W. Breed, T. L. Jensen, and P. R. Buseck, 2014: Individual aerosol particles in ambient and updraft conditions below convective cloud bases in the Oman mountain region. *J. Geophys. Res. Atmos.*, **119**, 2511–2528, <https://doi.org/10.1002/2013JD021165>.
- Squires, P., 1958: The microstructure and colloidal stability of warm clouds. *Tellus*, **10**, 256–261, <https://doi.org/10.1111/j.2153-3490.1958.tb02011.x>.
- Taylor, J. W., and Coauthors, 2016: Observations of cloud microphysics and ice formation during COPE. *Atmos. Chem. Phys.*, **16**, 799–826, <https://doi.org/10.5194/acp-16-799-2016>.
- Twomey, S., and P. Squires, 1959: The influence of cloud nucleus population on the microstructure and stability of convective clouds. *Tellus*, **2**, 408–411, <https://doi.org/10.3402/tellusa.v11i4.9331>.
- Wall, C., C. Liu, and E. Zipser, 2013: A climatology of tropical congestus using CloudSat. *J. Geophys. Res. Atmos.*, **118**, 6478–6492, <https://doi.org/10.1002/jgrd.50455>.
- Wehbe, Y., and Coauthors, 2021: Analysis of aerosol–cloud interactions and their implications for precipitation formation using aircraft observations over the United Arab Emirates. *Atmos. Chem. Phys.*, **21**, 12 543–12 560, <https://doi.org/10.5194/acp-21-12543-2021>.
- Wildeman, S., S. Sterl, C. Sun, and D. Lohse, 2017: Fast dynamics of water droplets freezing from the outside in. *Phys. Rev. Lett.*, **118**, 084101, <https://doi.org/10.1103/PhysRevLett.118.084101>.
- Woods, S., and Coauthors, 2018: Microphysical properties of tropical tropopause layer cirrus. *J. Geophys. Res. Atmos.*, **123**, 6053–6069, <https://doi.org/10.1029/2017JD028068>.